arXiv:astro-ph/9912503v2  27 Apr 2000

# NON-CIRCULAR GAS KINEMATICS AND STAR FORMATION
## IN THE RINGED GALAXY NGC 4736

TONY WONG AND LEO BLITZ
Astronomy Department and Radio Astronomy Laboratory, University of California, Berkeley, CA 94720

*accepted 17 April 2000 by ApJ*

## ABSTRACT

We analyze the gas kinematics and star formation properties of the nearby RSab galaxy NGC 4736 using interferometric and single-dish CO(1-0) data and previously published H$\alpha$ and H I data. The CO morphology is dominated by a central molecular bar and tightly wound spiral arms associated with a bright ring of star formation. Strong H I emission is also found in the ring, but H I is absent from the central regions. Comparison of the H I and H$\alpha$ distributions suggests that H I in the ring is primarily dissociated H$_2$. Modeling of the CO kinematics reveals gas motion in elliptical orbits around the central bar, and we argue that the ring represents both the OLR of the bar and the ILR of a larger oval distortion. The H I kinematics show evidence for axisymmetric inflow towards the ring and are inconsistent with streaming in aligned elliptical orbits, but the highly supersonic ($\sim$40 km s$^{-1}$) inflow velocities required, corresponding to mass inflow rates of $\sim$2 M$_\odot$ yr$^{-1}$, suggest that more sophisticated models (e.g., gas orbiting in precessed elliptical orbits) should be considered. The radial CO and H$\alpha$ profiles are poorly correlated in the vicinity of the nuclear bar, but show a better correlation (in rough agreement with the Schmidt law) at the ring. Even along the ring, however, the azimuthal correspondence between CO and H$\alpha$ is poor, suggesting that massive stars form more efficiently at some (perhaps resonant) locations than at others. These results indicate that the star formation rate per unit gas mass exhibits strong spatial variations and is not solely a function of the available gas supply. The localization of star formation to the ring is broadly consistent with gravitational instability theory, although the instability parameter $Q \sim 3$ on average in the ring, only falling below 1 in localized regions. Large-scale dynamical effects, by concentrating gas at resonances and influencing the star formation rate, appear to play a key role in this galaxy's evolution.

*Subject headings:* galaxies: evolution — galaxies: ISM — galaxies: individual (M 94, NGC 4736) — ISM: kinematics and dynamics — stars: formation

## 1. INTRODUCTION

The process of star formation in present-day galaxies, although still poorly understood, appears to require the accumulation of significant amounts of cold neutral gas. Thus, in galaxies where star formation is concentrated in distinct structures such as rings, the cold gas is also found concentrated in such structures, as revealed by high-resolution radio interferometry (see review by Kenney 1997). Exceptional examples of such rings include those in NGC 4314 (Benedict, Smith, & Kenney 1996) and NGC 4321 (Sakamoto et al. 1995). Two key questions that are raised by the study of these systems are the following: what are the physical processes that lead to the formation of gaseous ring structures, and how does gas accumulation ultimately lead to star formation?

In the usual interpretation of dynamical rings (where no collision between galaxies is indicated), a rotating bar or oval distortion induces a radial flow of gas toward orbital resonances, leading to ring formation. While this explanation has been lent considerable support by numerical simulations (Schwarz 1981; Combes & Gerin 1985; Byrd et al. 1994) as well as observations that show that rings are preferentially found in barred galaxies (see review by Buta & Combes 1996), direct kinematic evidence that bars drive *net* radial flows has been lacking. Indeed this is hardly surprising: Kenney (1994) has pointed out a number of problems with measuring gas inflow rates directly, among

them the tendency for gas in a barred potential to follow elliptical orbits that can mimic net inflow when only the line-of-sight velocity component is observed. As a result, inflow rates have been calculated only indirectly, by comparison with hydrodynamic models (Regan, Vogel, & Teuben 1997) or by estimating the gravitational torque exerted by the stellar potential on the gas (Quillen et al. 1995). These studies have yielded net inflow velocities of $\sim$10–20 km s$^{-1}$.

Once gas is available, are there general "laws" that govern the rate at which it is converted into stars? Kennicutt (1989) investigated this question from a primarily global perspective, using disk-averaged quantities to derive a Schmidt (1959) type law, in which the star formation rate (SFR) per unit area is roughly proportional to a power $N \sim 1.5$ of the gas surface density ($\Sigma_{SFR} \propto \Sigma_{gas}^N$). Yet he found that a simple power law tended to overpredict the SFR in the outer parts of galaxies, and consequently revived a suggestion by Quirk (1972) that star formation could only occur in regions where the gas density exceeded a critical threshold for gravitational instability. In this scenario, a controlling factor in star formation lies in the large-scale properties of the galaxy disk, in contrast to theories in which star formation is regulated by conditions in the local environment (e.g. Dopita 1985). Further observations, at higher spatial and velocity resolution than those available to Kennicutt (1989), should provide a clear test of

the generality of the Schmidt law and the star formation threshold, distinguishing them from alternative star formation laws that depend on the orbital frequency (Wyse & Silk 1989) or tidal shear (Kenney, Carlstrom, & Young 1993).

A puzzling result also highlighted by Kennicutt (1989) is the lack of correlation between disk-averaged Hα and CO line intensities; indeed, he found a substantially better correlation between Hα and H I emission. Two explanations were suggested: a variation in the CO-to-H$_2$ conversion factor (hereafter the "X-factor", following Bloemen et al. 1986), or a bimodal star formation process that leads to low-mass star formation being more strongly coupled to the molecular gas than high-mass star formation. More recently, Elmegreen (1993) has argued that both diffuse and self-gravitating molecular clouds can exist, and as a result the H$_2$ mass may be a poor indicator of star formation. Although these ideas may be difficult to test observationally, a simple comparison of how H I and CO are distributed *within* galaxies—relative to recent star formation—may provide clues as to why, on large scales, CO appears to be only weakly correlated with star formation.

Motivated by these questions, we have undertaken a detailed study of the gas kinematics and star formation in NGC 4736, a nearby ($d = 4.2$ Mpc using $H_0 = 75$ km s$^{-1}$ Mpc$^{-1}$) Sab galaxy with a bright ring of star formation about $45''$ (1 kpc) from its center. A faint outer ring, about $5'$ (6 kpc) in radius, is also seen in deep optical images (Sandage 1961). Previous H I synthesis observations (Bosma, van der Hulst, & Sullivan 1977) and optical and near-infrared imaging (Möllenhoff, Matthias, & Gerhard 1995, hereafter MMG95) have demonstrated that the disk of the galaxy is non-axisymmetric, and hence the rings may occur at the inner and outer Lindblad resonances (ILR and OLR) of an oval potential (Gerin, Casoli, & Combes 1991). In addition, MMG95 have suggested that the inner ring may coincide with the OLR of a central stellar bar, $\sim 30''$ in extent, seen in optical and near-infrared isophotes. We summarize the basic observational parameters of the galaxy in Table 1.

Table 1. Global Properties of NGC 4736

| Parameter | Value | Ref. |
|---|---|---|
| Right ascension (J2000) | $12^h 50^m 53\overset{s}{.}06$ | 1 |
| Declination (J2000) | $41°07'13\overset{''}{.}65$ | 1 |
| Morphological type | (R)SA(r)ab | 2 |
| Systemic LSR velocity | 315 km s$^{-1}$ | 3 |
| Adopted distance, $d$ | 4.2 Mpc | 3 |
| Angular scale | $1'' = 20$ pc | 3 |
| Inclination, $i$ | $35°$ | 4 |
| Position angle, $\phi_{maj}$ | $\sim 295°$ | 3 |
| Optical diameter, $D_{25}$ | $11\overset{'}{.}2$ (13.5 kpc) | 2 |

(1) Becker, White, & Helfand 1995; (2) de Vaucouleurs et al. 1991; (3) This paper; (4) Möllenhoff et al. 1995.

The nucleus of NGC 4736 has also been studied intensively. Classified as a LINER based on optical emission lines (Heckman 1980), several indications suggest that it harbors an active galactic nucleus (AGN): a compact nu-

clear source has been detected at 5 and 15 GHz ($1''$ resolution, Turner & Ho 1994), with a spectral index indicative of synchrotron emission, as well as in the ultraviolet with *HST* ($0\overset{''}{.}1$ resolution, Maoz et al. 1995), and the X-ray with the *ROSAT* PSPC ($\sim 30''$ resolution, Cui, Feldkhun, & Braun 1997). The lack of emission lines and dust features in the 8–13 $\mu$m spectrum led Roche & Aitken (1985) to conclude that there was relatively little star formation occurring in the nucleus. However, the presence of strong Balmer absorption lines indicative of A-type stars (Pritchet 1977) and strong CO absorption indicative of young red giants (Walker, Lebofsky, & Rieke 1988) suggests that a nuclear starburst occurred roughly 1 Gyr ago. If NGC 4736 indeed harbors an AGN and recent starburst, it would be an important testbed for theories relating nuclear bars to the fueling of nuclear activity (e.g., Simkin, Su, & Schwarz 1980; Shlosman, Frank, & Begelman 1989).

The results of our investigation are presented as follows. §2 describes our new CO observations and the H I and Hα datasets used for comparison. §3 compares and contrasts the distribution of atomic and molecular gas in this galaxy, revealing some striking differences in both the radial and azimuthal profiles. In §4 we discuss the gas kinematics as traced by CO and H I and compare them with simple models of radial inflow, a warp in the disk, and oval orbits. In §5 we analyze the star formation rate and its relation to the observed gas density. The results and implications of this work are discussed in §6, and our conclusions are summarized in §7. Preliminary results from this study have appeared in Wong & Blitz (1999).

## 2. OBSERVATIONS AND DATA REDUCTION

### 2.1. *BIMA CO Observations*

Observations with the Berkeley-Illinois-Maryland Association[1] (BIMA) interferometer were conducted in 1996 October and 1997 April in the C array configuration (projected baselines 2.2–36 kλ) with 9 antennas. Additional observations in the D configuration (2.3–11 kλ) with 10 antennas were made in 1999 July and August as part of the BIMA Survey of Nearby Galaxies (BIMA SONG). To ensure that the entire Hα ring was imaged, a 7-pointing hexagonal mosaic was observed, with the pointings separated by $50''$ (half of the primary beam FWHM). This provides fairly uniform sensitivity out to a radius of $\sim 50''$. The total on-source observing time was 25 hours.

The receiver was tuned to the CO ($J = 1 \rightarrow 0$) transition at 115.2712 GHz ($\lambda = 2.6$ mm), and the correlator was configured to have 4 independently positioned spectral windows, each with 100 MHz bandwidth and 64 channels. The LSR velocity range covered was 150–650 km s$^{-1}$ at a resolution of 4.06 km s$^{-1}$. The typical SSB system temperature corrected to above the atmosphere ($T^*_{sys}$) was 400–600 K on all tracks.

The data were calibrated and reduced using the MIRIAD package (Sault, Teuben, & Wright 1995). An online linelength calibration was applied to correct for variations in the length of the signal path from the antenna to the correlator; remaining drifts in the antenna phase gains were then corrected by observing the nearby quasar 1310+323 every half hour and fitting a low-order polynomial to the antenna-based self-calibration solutions.

Flux calibration was performed using observations of Mars taken on each track. A bandpass measurement was made on 3C273 for each track, to verify that the online bandpass calibration was working properly. Following the initial calibration, the data were subjected to an additional round of phase-only self-calibration using a deconvolution model.

The uncertainty in the flux scale is likely to be dominated by the effects of atmospheric phase decorrelation. Although the Mars observations, when phase-corrected over very short ($\sim$1 s) timescales, provide a measurement of the antenna gains to within a few percent (apart from uncertainties in the Martian flux model), rapid phase correction cannot likewise be applied to the source data. Hence the source flux will be attenuated when averaged over time. To make a partial correction for decorrelation, we have instead derived the antenna gains by a bootstrap method: a comparison with Mars was used to derive an estimate for the flux of 1310+323, and this value was then compared to the visibility amplitudes of the 1310+323 data, when averaged over 6-minute timescales, to derive the antenna gains. The resulting gains should scale up the amplitudes for antennas that share many long baselines and thus suffer greater decorrelation. Comparison of source spectra from the four best tracks suggests an uncertainty of $\lesssim$20% in the flux scale; the uncertainty is somewhat larger for the poorer tracks, but data from those tracks is weighted less due to their high noise variance.

After calibration of the visibilities, two datacubes were produced with 10 km s$^{-1}$ channels, one with a robust weighting (Briggs 1995), which provides a good compromise between the sensitivity of natural weighting and the resolution and sidelobe suppression of uniform weighting, and the second with a Gaussian taper applied to weight down the longer baselines. These will be referred to as the "robust" and "tapered" datacubes respectively. The cubes were deconvolved using a variant of the CLEAN algorithm developed by Steer, Dewdney, & Ito (1984) to improve the deconvolution of spatially extended emission, and implemented in the MIRIAD task MOSSDI. The robust datacube had a resolution of $6.''86 \times 5.''02$ (FWHM of synthesized beam). The tapered datacube, although having poorer resolution ($15''$), was more sensitive to extended structure and less affected by atmospheric decorrelation and resulting calibration errors because it emphasizes shorter baselines. (For these observations the "short-baseline" data come primarily from antennas that were physically close together, not from projection effects due to low source elevation.) The rms noise in the robust and tapered datacubes were roughly 70 and 80 mJy beam$^{-1}$ (190 and 33 mK) respectively for each 10 km s$^{-1}$ channel.

## 2.2. Kitt Peak CO Observations

Single-dish CO observations were performed in 1997 June at the NRAO[2] 12 m telescope on Kitt Peak, Arizona. With the 3 mm SIS receivers, typical system temperatures were 300–400 K. Spectra from orthogonal polarizations were recorded by two 256-channel filterbanks (one for each polarization) with a channel width of 2 MHz (5.2 km s$^{-1}$). Calibration was performed using the chopper wheel method (e.g., Kutner & Ulich 1981) approximately

every 20 minutes. Pointing was checked approximately every 2–2.5 hours with observations of Mars; the typical change in pointing offsets was $8''$ (rms) and ranged from $3''$ to $12''$.

A total of 43 grid points were observed, comprising a $7 \times 7$ square grid centered on NGC 4736 with 3 points each at the NE and SW corners omitted. The spacing of the grid was $27''$, approximately half of the FWHM of the primary beam. Nyquist sampling of all spatial frequencies ("baselines") from 0 to 12 m requires a grid spacing of $\lambda/2D = 22''$; nonetheless, because the dish illumination falls to zero towards the edges, the amount of signal aliased by our undersampling should be small. On-source integration time was typically 10 minutes for the inner 5 $\times$ 5 grid points ($1.'8 \times 1.'8$) and 4 minutes for the outer points.

Spectra were output on the $T_R^*$ scale, which represents the source antenna temperature corrected for ohmic losses, atmospheric absorption, spillover, and scattering (Kutner & Ulich 1981). Linear baselines were fit to line-free channels of the spectra and subtracted; higher-order variations in the baseline were generally not seen. The resulting datacube (hereafter the "KP cube") had an rms noise of 11 mK in each 5.2 km s$^{-1}$ channel. The $T_R^*$ temperatures were converted to Janskys using a nominal telescope gain of 33 Jy K$^{-1}$. This gain is strictly appropriate for point sources only; it was found that the fluxes had to be scaled up by 10% to produce a more satisfactory combination with the BIMA data.

## 2.3. Combining the BIMA and KP Data

The total CO flux measured in the KP cube was 1620 Jy km s$^{-1}$, which is comparable to the flux of 1600 Jy km s$^{-1}$ detected by Gerin et al. (1991) using the IRAM 30 m telescope. For comparison, the tapered BIMA cube recovered a flux of 1000 Jy km s$^{-1}$, $\sim$60% of the total flux, while the robust BIMA cube recovered a flux of 620 Jy km s$^{-1}$. These results illustrate that deconvolution errors, which become more severe at higher resolution because of greater decorrelation, can affect the CLEAN algorithm's ability to recover the actual flux.

Two techniques were employed to combine the interferometer and single-dish data. In the "linear combination" technique, the BIMA and KP data are combined in the image plane before deconvolution, and then deconvolved with a composite beam, as described by Stanimirović et al. (1999). In the "Fourier" technique, implemented in the MIRIAD task IMMERGE, the KP and deconvolved BIMA maps are transformed to the Fourier plane, and low spatial frequencies in the BIMA maps are partially replaced by single-dish data in the inner part of the Fourier plane. The results of the two methods agreed well (cf. discussion below), especially considering the inherent limitations of the data (uncertain relative flux calibration, single-dish pointing errors, etc.). Further discussion of techniques for combining single-dish and interferometer data and their application to the BIMA SONG will follow in a future paper (Regan et al. 2000, in preparation).

Following the data combination, an integrated intensity (hereafter "moment-0") map for each cube was made by

first smoothing each datacube to 20″ (robust) or 30″ (tapered) resolution and masking out regions in the original cube where the signal fell below the $3\sigma$ level in the smoothed cube. The channel maps of the original cube were then summed, including only unmasked pixels that rose above the $1\sigma$ level. Although this masking technique introduces some bias against finding isolated compact emission in the datacube, it is valuable in practice because the emission at any given point in the galaxy is generally confined to a small number of spectral channels, and will be strongly attenuated if the noise from all of the channels is added in.

The line-of-sight velocity field was derived by making Gaussian fits to the spectrum at each pixel of the datacube. This provides greater robustness than a first moment map, which can be strongly affected by noise in outlying channels (for a full discussion see Wong 2000), without having to impose an arbitrary mask or clipping level. The assumption that the profiles are Gaussian was found to be a reasonable one: inspection of the profiles for the robustly weighted cube showed no clear indication of double-peaked profiles, although asymmetries in profiles near the center do occur as a result of beam smearing of the galaxy's rotation. To reduce noise in the velocity field, only Gaussian fits with integrated intensities of $>6$ Jy beam$^{-1}$ km s$^{-1}$ and uncertainties in mean velocity of $<20$ km s$^{-1}$ were included.
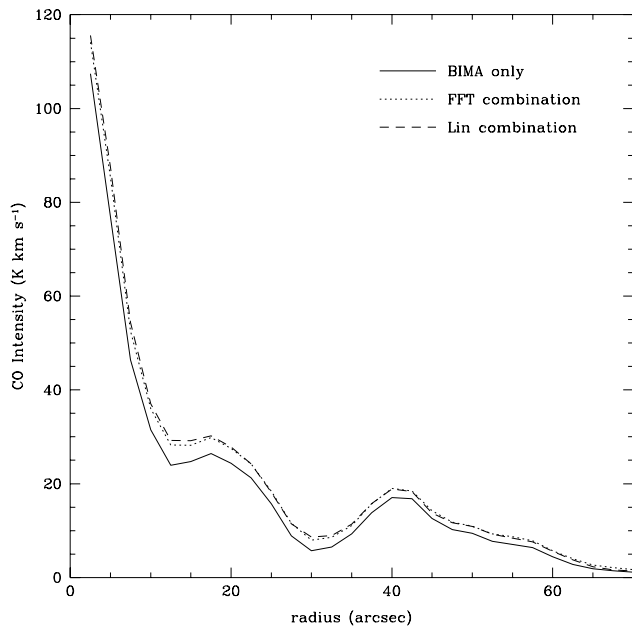


FIG. 1.— Radial CO profiles, averaged in 2″.5-wide elliptical rings, for the BIMA-only robustly weighted data, as well as the combined (KP+BIMA) data using two data combination techniques (the "Fourier" method and the "linear combination" method, see text). No inclination correction has been made.

In Figure 1 we compare the radial CO profiles derived from the BIMA-only moment-0 maps to those derived from each of the two data combination techniques. Not only do the two combination methods show good agreement, but the inclusion of the single-dish data has surprisingly little impact on the radial profile. Two factors appear to be responsible for this result. First of all, due to the short

baselines provided by BIMA, only very extended ($>30″$), low surface brightness structure is resolved out, resulting in little change to the *shape* of the profile over the region observed. This also implies that the derived velocity field is relatively insensitive to the inclusion of the single-dish data, since it is weighted toward high-brightness regions. Secondly, the low measured fluxes in the BIMA cube are mainly due to large-scale negative regions in the channel maps that are anticorrelated with the actual emission, and have therefore been excluded in the process of forming the moment-0 map. (These negative regions result from imperfect deconvolution, probably due to residual calibration errors and phase decorrelation.) As a result, while the inclusion of the single-dish data has a noticeable impact on the flux of each channel map, it has much less effect ($\lesssim 20\%$) on the flux of the moment-0 map, even for the robust datacube. Constructing the moment-0 maps using Gaussian fits instead yielded similar results.

In this paper we perform our analysis on the moment-0 maps and velocity fields generated with the Fourier combination method. The corresponding channel maps from the robust and tapered cubes are shown in Figures 2 and 3 respectively. As discussed above, it would make little difference if we used the linear combination method or even the BIMA-only maps for our analysis, since their fluxes agree within the $\sim 20\%$ calibration uncertainties, not to mention the potentially much larger uncertainties in the X-factor. The differences in the velocity fields are similarly quite small ($<4$ km s$^{-1}$) except near the nucleus where the profiles are broad and the mean velocity is more uncertain.

### 2.4. *Hα Data*

We were kindly provided with Hα+[N II] images from a number of sources, including Pogge (1989) and González Delgado et al. (1997). For this study we have used the image of Pogge (1989), taken with the Lick 1 m telescope in 1987, which provides a field of view ($4'.5 \times 4'.5$) comparable to our BIMA observations. Absolute fluxes for this image are given by Smith et al. (1991), who derived Hα fluxes of $8.3 \times 10^{-12}$ erg s$^{-1}$ cm$^{-2}$ for the ring ($r=30″$–$60″$) and $1.2 \times 10^{-11}$ erg s$^{-1}$ cm$^{-2}$ for the entire image. Astrometric coordinates were derived by comparison with a VLA 1.4 GHz image provided by N. Duric (Duric & Dittmar 1988) and are accurate to $2″$. Of some concern is the much stronger emission in the nuclear region found by González Delgado et al. (1997) relative to Pogge (1989): the former finds that 15% of the flux within $r=60″$ lies within $r=15″$, while the latter finds only 3.3%. The continuum subtraction may be more reliable in Pogge's image, since the line-free continuum was measured at 6435 Å rather than 5960 Å; furthermore, the integrated Fabry-Pérot image of Mulder (1995), which excludes [N II] from the LINER, also shows very little Hα near the nucleus. Nonetheless, given that the effects of [N II] emission, stellar Hα absorption, and dust extinction will all be most severe at the nucleus, caution must be exercised in drawing conclusions about the SFR in the nuclear region from an Hα image (see §5).

### 2.5. *H I Data*

A VLA H I datacube for NGC 4736 was provided courtesy of R. Braun (Braun 1995). The observations were taken in 1989–90 in the B, C, and D configurations; with
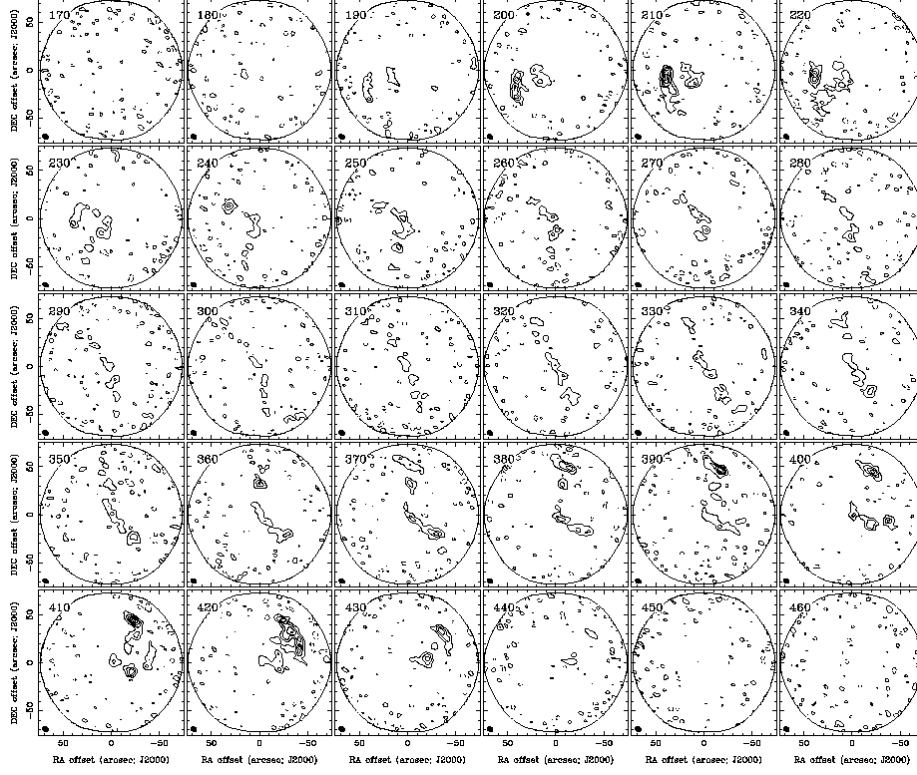
Fig. 2.— Robustly weighted channel maps of CO emission in NGC 4736. Contours are spaced by $3\sigma$ starting at $2\sigma$, where $\sigma=0.07$ Jy bm$^{-1}$. Maps have been primary beam corrected within the region shown, so contours represent absolute fluxes. The synthesized beam, shown in the lower left corner of each panel, has a FWHM of $6\rlap{.}''9 \times 5\rlap{.}''0$. The LSR velocity of each plane is shown in the upper left.
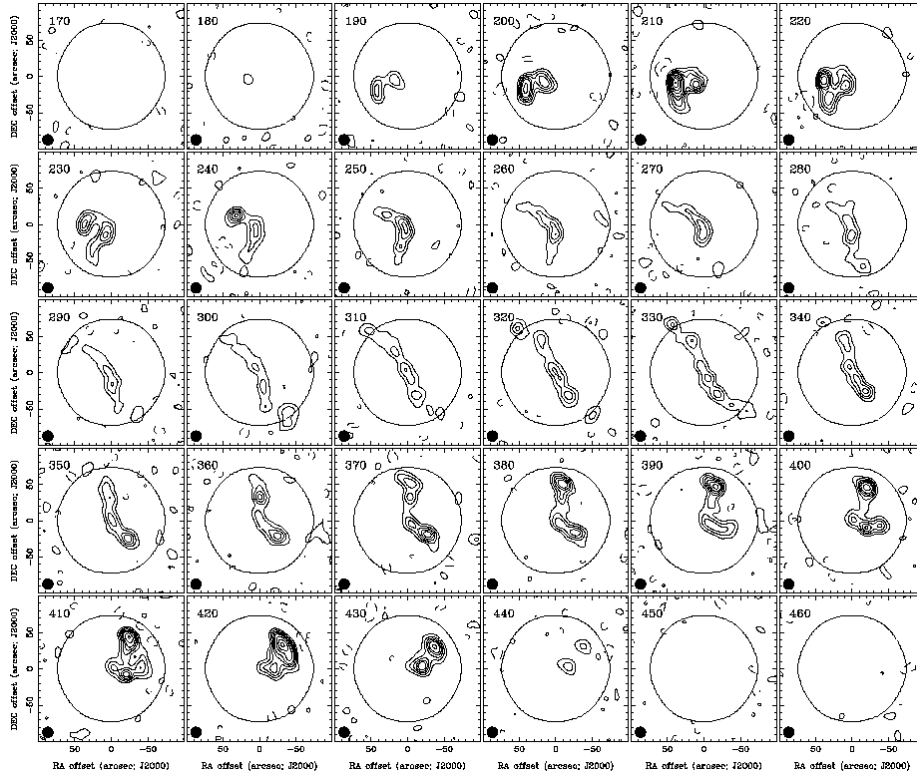


Fig. 3.— Channel maps of CO emission in NGC 4736 at $15''$ resolution. Contours are spaced by $3\sigma$, where $\sigma=0.08$ Jy bm$^{-1}$. Maps have been primary beam corrected within the region enclosed by the circular contour; absolute fluxes are unreliable outside of this contour.

uniform weighting, a resolution of $\sim 6''$ was achieved. The cube used here was smoothed to a resolution of $15''$, resulting in an rms noise in each 5.2 km s$^{-1}$ channel of about 1.7 mJy bm$^{-1}$ or 4.6 K. The integrated intensity and line-of-sight velocity maps were constructed from the deconvolved datacube in the same way as for the CO data (§2.1). The total fluxes in the cube and moment-0 maps were 90 and 57 Jy km s$^{-1}$ respectively, indicating that the masking technique missed some of the flux in the cube. However, in the inner $5' \times 5'$, the region of interest for this study, the agreement is substantially better (31 Jy km s$^{-1}$ in the cube and 28 in the moment-0 map). Although single-dish data were not included (a single-dish flux of 94±5 Jy km s$^{-1}$ was measured by Huchtmeier & Seiradakis 1985), the inclusion of a D-array mosaic at $65''$ resolution provides sensitivity to most of the extended flux, especially in the inner regions of the galaxy where the emission in any one velocity channel is spatially confined due to the rotation of the galaxy.
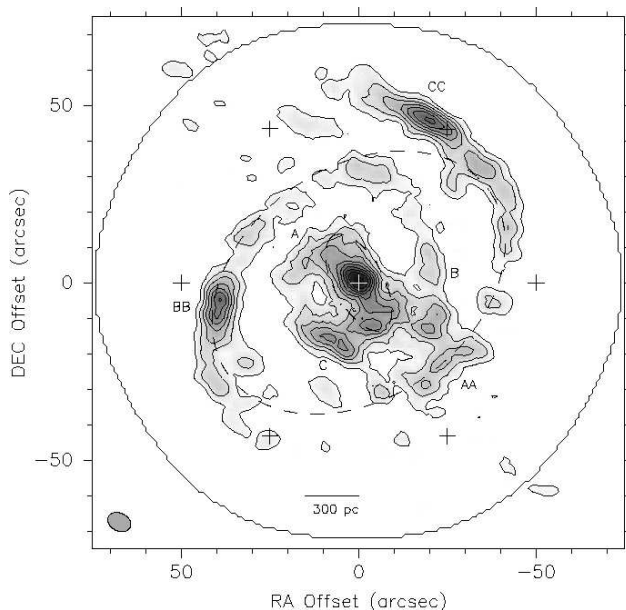
## 3. DISTRIBUTION OF THE NEUTRAL GAS



FIG. 4.— Integrated intensity map derived from the robustly weighted CO datacube. The contours are spaced by 4.5 Jy bm$^{-1}$ km s$^{-1}$. The crosses represent the pointing centers of the mosaic, and the outer contour is the boundary of the region that has been primary-beam corrected (corresponding to $\geq 56\%$ of the central sensitivity). Several of the major gas complexes are labeled to highlight the threefold symmetry of the CO distribution (see text). Prominent optical features (the nuclear bar and the H$\alpha$ ring) are drawn as ellipses.

### 3.1. Integrated Intensity Images

The moment-0 image for the robustly weighted CO cube is shown in Figure 4. Our map is generally consistent with previous CO observations by Gerin et al. (1991) using the IRAM 30 m and Sakamoto et al. (1999) using the Nobeyama Millimeter Array. We note that the combination of high angular resolution and a large field of view in the BIMA map allow for a much clearer view of CO emission in the ring than has been previously available. Moving outward from the center, the CO morphology is

characterized by a strong central peak, an elongated feature (the "molecular bar"), arc-like extensions from the ends of the bar, and tightly wound arms that are associated with the H$\alpha$ ring (outer dashed ellipse).

The bar.—That the apparent "bar" is a true distortion in the potential of the galaxy is not obvious from the CO image, but is confirmed by near-infrared images (MMG95; Block et al. 1994a) and the kinematic analysis presented in §4. There is no clear indication of an angular offset between the stellar bar (inner dashed ellipse) and its molecular counterpart, although the gas bar may be trailing slightly. This contrasts with the general expectation that the gas bar will lead the stellar bar, based on numerical simulations (Combes & Gerin 1985; Sanders & Tubbs 1980) and a number of previous observations (e.g., NGC 7479, Quillen et al. 1995; M101, Kenney, Scoville, & Wilson 1991).

Arc-like extensions from the bar.—These features extend azimuthally from the bar ends and exhibit a complex morphology. One interpretation is that a single spiral arm begins at the northern end of the bar (labeled A in Figure 4), wraps around by 270° to point B, and merges into the ring CO component. Alternatively, the arm beginning at A may merge with the ring at point AA, and the emission at B could be associated with a distinct spiral arm beginning at the southern end of the bar. Optical/near-infrared color index maps (MMG95; Block et al. 1994b), which trace the distribution of cold dust, appear to show a continuous spiral arm that does not approach the ring until it has wrapped around to the northern side, thus favoring the first interpretation. Note the gap in CO brightness between the bar+spiral arm region and the ring.

CO in the ring.—While the H$\alpha$ ring morphology might be described as a pointy oval, the clumpy CO emission in this region traces a pair of tightly wound spiral arms, which on the northern side extends well outside the ring. These arms are continuous with the H I arms seen in the maps presented by Braun (1995). Apparent ring features formed by tightly wound spiral arms, dubbed "pseudorings," are commonly found in galaxies (de Vaucouleurs & Buta 1980), and support the interpretation that galactic rings are manifestations of spiral density waves (Buta & Combes 1996).

Also notable in Figure 4 is the lack of twofold symmetry in the CO brightness. Whereas the locations at which the CO arms depart from the ring are approximately symmetric, reflecting the twofold symmetry of the H I arms which they are continuous with, the locations of peak emission along these arms do not show this symmetry. Rather, there is a noticeable threefold symmetry in the CO intensity distribution, with emission peaks labeled A, B, and C in the inner disk (Figure 4) lying opposite to the peaks labeled AA, BB, and CC in the ring. We discuss the azimuthal symmetries in the ring further in §5.3 and §6.3.1.

Contours of integrated H I emission are overlaid on a greyscale image of the CO emission in Figure 5. In contrast to the CO, the H I distribution in the ring is strongly bisymmetric. Atomic gas is largely absent interior to the ring, where most of the gas is molecular, and even within the ring the CO and H I peaks avoid each other, with the possible exception of the H I peak in the northwest (upper right of Fig. 5). This detailed anticorrelation was already
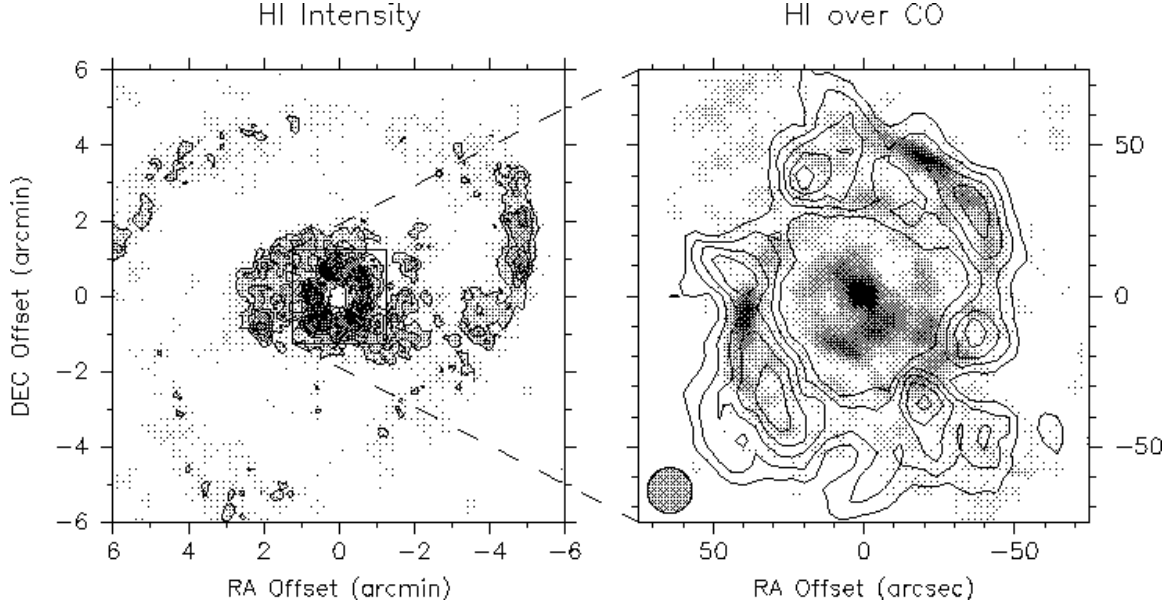
FIG. 5.— H I integrated intensity image (contours spaced by 70 mJy bm$^{-1}$ km s$^{-1}$ starting at 140) overlaid on CO intensity image (greyscale). The 15″ H I beam is shown on the lower left.

hinted at by Gerin et al. (1991) based on lower resolution data and is unexpected if one assumes that molecular clouds are associated with regions of excess H I column density. Rather, it suggests that the H I peaks may represent regions where molecular gas has been dissociated by UV radiation and has not yet recombined to form H$_2$, a possibility that is discussed in §6.4.

### 3.2. Radial Gas Profiles

The radial profiles of H I and H$_2$ surface density at 15″ resolution are plotted in Figure 6 on a log-linear plot. Also shown is the radial profile of the $K_s$-band (2.2 $\mu$m) light, wth arbitrary scaling, derived from a Two Micron All Sky Survey (2MASS) Atlas image smoothed to 15″ resolution. For $r \leq 60''$, the unsmoothed $K_s$ profile from the 2MASS image is consistent with the profile derived by MMG95 from a more sensitive 2.2 $\mu$m image.
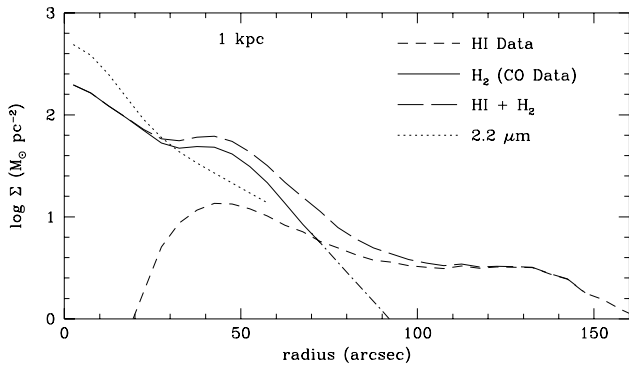


FIG. 6.— Azimuthally averaged radial gas profiles, corrected for inclination and including helium, on a logarithmic scale. The stellar light profile at 2.2 $\mu$m is shown as a dotted line for comparison, with an arbitrary vertical offset. The CO profile has been extrapolated beyond 70″ (dash-dot line). All images are at 15″ resolution, hence the flattening near $r=0''$.

In converting from CO brightness to H$_2$ column density

we have adopted an X-factor of:

$$N_{\mathrm{H}_2} = 2 \times 10^{20} \left( \frac{I_{\mathrm{CO}}}{\mathrm{K\ km\ s^{-1}}} \right) \mathrm{cm^{-2}} \ .$$

This is consistent with the value of $(1.9 \pm 0.2) \times 10^{20}$ cm$^{-2}$ (K km s$^{-1}$)$^{-1}$ estimated by Strong & Mattox (1996) from diffuse Galactic $\gamma$-ray emission. The corresponding mass surface density is

$$\Sigma_{\mathrm{H}_2} = 2\, N_{\mathrm{H}_2}\, m_H\, \cos i$$
$$= 330 \left( \frac{I_{\mathrm{CO}}}{\mathrm{Jy\ km\ s^{-1}\ arcsec^{-2}}} \right) \cos i \quad \mathrm{M_\odot\ pc^{-2}},$$

where the conversion of 1 K$=9.6 \times 10^{-3}$ Jy arcsec$^{-2}$ has been applied for $\lambda=2.6$ mm. The analogous expressions for H I in the optically thin approximation are:

$$N_{\mathrm{HI}} = 1.82 \times 10^{18} \left( \frac{I_{21}}{\mathrm{K\ km\ s^{-1}}} \right) \mathrm{cm^{-2}} \ ,$$

$$\Sigma_{\mathrm{HI}} = N_{\mathrm{HI}}\, m_H\, \cos i$$
$$= 1.0 \times 10^4 \left( \frac{I_{21}}{\mathrm{Jy\ km\ s^{-1}\ arcsec^{-2}}} \right) \cos i \quad \mathrm{M_\odot\ pc^{-2}},$$

using the conversion 1 K$=1.5 \times 10^{-6}$ Jy arcsec$^{-2}$. For both H I and CO profiles, the galaxy has been assumed to have an inclination $i=35°$ (MMG95) and a position angle $\phi=295°$ (§4.1).

The total gas surface density (corrected for helium) is then given by:

$$\Sigma_{\mathrm{gas}} = 1.36(\Sigma_{\mathrm{HI}} + \Sigma_{\mathrm{H}_2}),$$

a quantity which is independent of the adopted distance. Note that the H I + H$_2$ profile in Figure 6 includes an extrapolation of the CO profile by an exponential with scalelength 11″.5 (dot-dashed line), in order to avoid a spurious kink in the H I + H$_2$ profile resulting from the fact that the CO data are less sensitive than the H I data to the same gas surface density. (The CO observations at 15″ resolution detect, at the 3$\sigma$ level in each of two consecutive channels, surface densities down to $\sim$5 M$_\odot$ pc$^{-2}$
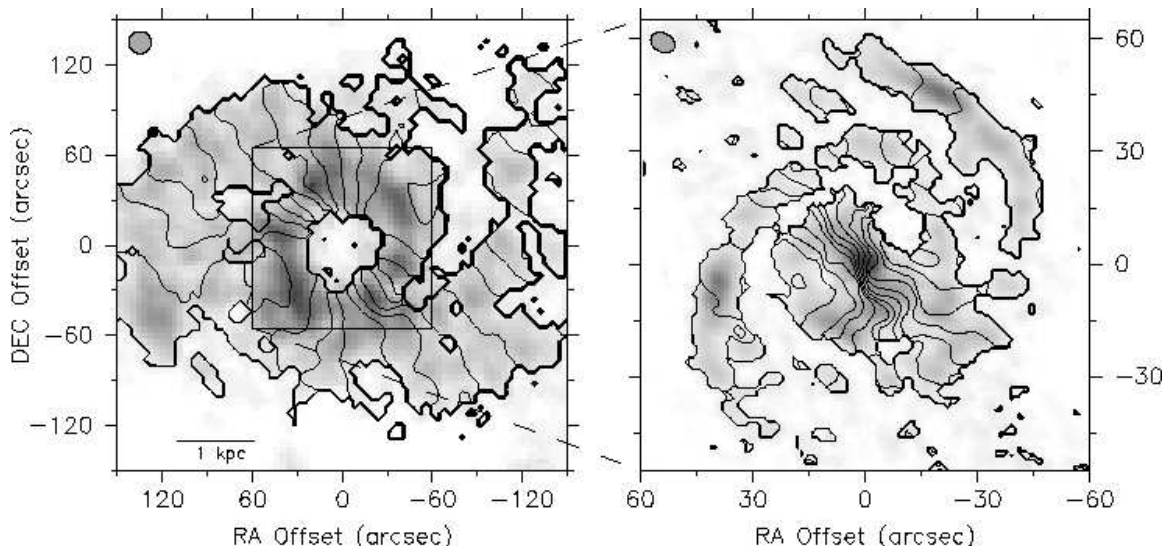
FIG. 7.— H I (*left*) and CO (*right*) line-of-sight velocity maps. The contours are spaced by 20 km s$^{-1}$ and range from 170 km s$^{-1}$ (east side) to 450 km s$^{-1}$ (west side).

when corrected to face-on, a factor of 3 higher than the H I limit.) The extrapolated H$_2$ mass is $1.1 \times 10^7$ M$_\odot$, less than 10% of the $1.7 \times 10^8$ M$_\odot$ of H$_2$ (excluding helium) measured within $r=70''$. When convolved to the appropriate resolution, our radial profiles agree well with previous observations of H I by Mulder & van Driel (1993) using the WSRT, and of CO by Gerin et al. (1991) using the IRAM 30 m.

The assumption that H I is optically thin is widely made in extragalactic astronomy, although Braun (1997) has argued that emission from dense, cool clouds in the inner disks of galaxies are likely to be optically thick, leading to an underestimate of the column density by factors of $\sim$2 (Walterbos & Braun 1996). In his high-resolution datacube for NGC 4736, Braun (1995) finds maximum emission brightness temperatures of $\sim$100 K, comparable to the thermal temperatures of cool H I clouds. Our adopted radial profile should therefore be considered a *lower limit* to the true H I surface density, although the correction is unlikely to be large since at $15''$ ($\sim$300 pc) resolution we are averaging over both cold and warm clouds. The adoption of a "standard" Galactic value for the X-factor is considerably more uncertain, and has been shown to underestimate the H$_2$ mass in the Magellanic Clouds and other low-metallicity galaxies (Wilson 1995) while possibly overestimating the mass near the Galactic Center by up to an order of magnitude (Sodroski et al. 1995; Dahmen et al. 1998). Since our observations of NGC 4736 cover the central 1–2 kpc where the metallicity is at or above the solar value (Oey & Kennicutt 1993) and physical conditions may be similar to those in the Galactic Center, we expect that the H$_2$ surface density we derive to be an *upper limit* to the true value.

With these assumptions in mind, a comparison of the H I and CO profiles indicates that most ($\sim$75%) of the gas at the location of the ring ($r=45''$) is molecular. An exponential fit to the total gas profile gives a scalelength of $\sim$30$''$; however, the fit is rather poor due to the presence

of the ring at $45''$ and a "plateau" from $100''$–$130''$. These features suggest that gas may have been redistributed across the disk, as discussed in the following section. Comparison of the gas profiles to the $K_s$-band profile, which traces the stellar surface density, shows that for $r < 50''$ the stellar profile is considerably steeper than the gas profile. This is partly due to a secondary enhancement at the location of the ring which is much more prominent in the gas than in the stars. Even interior to the ring ($r < 30''$), however, the stellar profile is steeper, presumably due to a bulge component.

## 4. GAS KINEMATICS

### 4.1. *Rotation Curve*

The CO and H I velocity fields derived from the Gaussian fits are shown in Figure 7. The dominant signature of circular rotation is apparent, although there are clearly non-circular motions along the kinematic minor axis (systemic velocity contour), which runs almost north-south. Rotation curves were fit to the velocity fields using a tilted-ring model (Begeman 1989) as implemented in the program ROTCUR within the GIPSY software package (van der Hulst et al. 1992). In this model, the line-of-sight[3] velocity at each point is decomposed as

$$V(x,y) = V_{\rm sys} + v_{\rm rot}(r)\sin i \cos\theta \qquad (1)$$

where $V_{\rm sys}$ is the systemic velocity of the galaxy, $v_{\rm rot}(r)$ is the rotation velocity of a ring at radius $r$ from the center, $i$ is the inclination of the ring from face-on, and $\theta$ is the azimuthal angle in the plane of the galaxy, which depends on the location of the point in relation to the rotation center as well as the position angle in the sky of the receding major axis ($\phi$) and the inclination ($i$). We refer to $V_{\rm sys}$, $\phi$, $i$, and the rotation center ($x_0, y_0$) as the *disk parameters* because for a circularly rotating disk they are fixed at all radii.

To determine the disk parameters, the velocity field of the tapered CO cube was fit in annuli from $20''$–$60''$ in intervals of $5''$. Initial estimates for the rotation velocity,

---

[3] Throughout this paper we refer to measured Doppler velocities as *line-of-sight* velocities, since *radial* velocities could be interpreted as being in the plane of the galaxy. We also use $V$ to refer to Doppler velocities and $v$ to refer to velocities in the plane of the galaxy.

inclination, and position angle were taken from MMG95 and used to determine the rotation center and systemic velocity. Then the rotation velocity, center, and systemic velocity were fixed to determine the inclination and position angle, and the process was repeated to improve the estimates. Due to the low inclination of the galaxy, $v_{\rm rot}$ and $i$ are tightly coupled and could not be determined independently; we therefore fixed the inclination to a value of $35°$ as determined by MMG95 from surface photometry. The systemic velocity was found to be $315\pm4$ km s$^{-1}$ and the rotation center was consistent with a location at the position of the radio continuum nucleus (Table 1). The remaining disk parameter, $\phi_{kin}$ (also referred to as the kinematic position angle or PA), assumed an average value of $295°$, but showed a noticeable variation with radius, rising from $290°$ to $300°$ between $r = 25''$ and $60''$.

Fixing the disk parameters to their average values, the remaining free parameter, $v_{\rm rot}$, was determined by fitting to the velocity field of the robust CO cube for $r \leq 25''$ (where beam smearing in the tapered cube is significant) and the tapered CO cube from $r=30''$–$55''$. A $\cos\theta$ weighting was applied to emphasize points close to the major axis, and points within $30°$ of the minor axis were excluded from the fit. Fitting was performed for the approaching and receding halves of the galaxy separately as well as for the entire galaxy. No statistically significant differences were found between the rotation curves of the two halves.

Using the same disk parameters, $v_{\rm rot}(r)$ was then determined from the H I velocity field. Beyond $r=80''$ the rotation curve was derived from the H I data after smoothing to $45''$ resolution, in order to improve the signal-to-noise ratio. Figure 8 shows the adopted rotation curve, which is a composite of the CO and H I data at various resolutions assuming the same disk inclination and PA. Outside the CO disk ($r > 60''$), the derived rotation curves for the approaching and receding sides differ by as much as 25 km s$^{-1}$, yet these differences are still within the errors at these radii. The large error bars in the outer disk probably reflect a combination of decreasing azimuthal coverage and azimuthal streaming motions near the major axis.
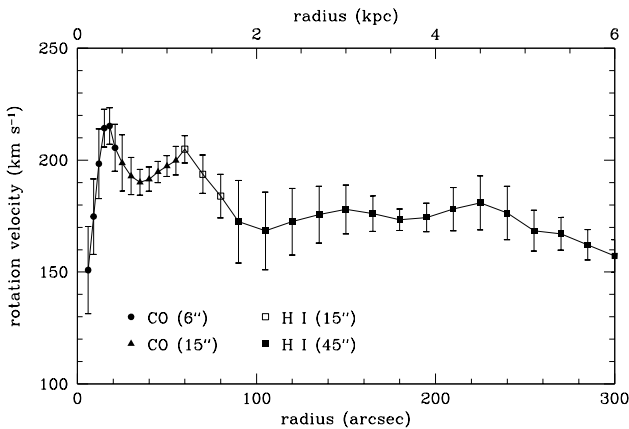


FIG. 8.— Adopted rotation curve for NGC 4736, derived from the $6''$ CO datacube for $r < 30''$, the $15''$ CO datacube for $30'' \leq r < 60''$, the $15''$ H I datacube for $60'' \leq r \leq 80''$, and the $45''$ H I datacube for $r > 80''$. An inclination of $35°$ has been taken into account.

The adopted rotation curve is characterized by a num-

ber of distinct humps and dips. The curve begins with a steep rise in the inner $15''$, with no correction having been applied for the effects of beam smearing or the influence of the nuclear bar. While the former will tend to soften the rise, the latter will tend to increase it, since the kinematic major axis is nearly orthogonal to the bar major axis. It is therefore likely that the first peak in $v_{\rm rot}$ at $r \approx 20''$ is due to gas moving in elliptical orbits aligned with the bar (§4.6). A secondary peak in $v_{\rm rot}$ at $r \approx 60''$, apparent in both the CO and H I datasets, also occurs in a region of strong streaming motions, especially on the southern side of the galaxy (§4.3). On the other hand, the rotation curve is already rising across the ring ($r=40''$–$50''$), where the gas motions are predominantly circular (see §4.2), suggesting that this second peak reflects a genuine mass concentration in the ring. This additional mass must be provided by stars, since the gas mass alone is only $\sim2\%$ of the dynamical mass at the radius of the ring. Consistent with this picture, MMG95 noted a "shelf" feature in their $K$ and $I$-band light profiles at $r=40''$, although it is hard to identify such a feature in the overall $K$ profile (Figure 6).
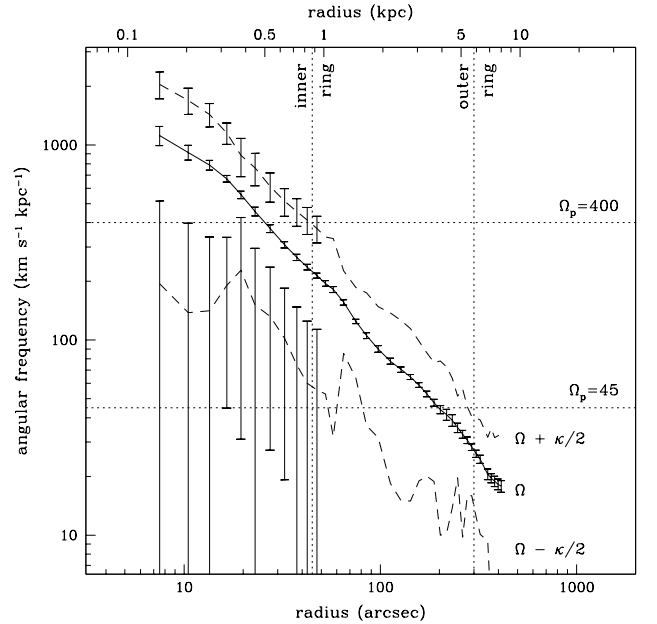


FIG. 9.— Resonance diagram showing radial variation of $\Omega$ and $\Omega \pm \kappa/2$ derived from the adopted rotation curve. The locations of the inner and outer rings are shown, as well as the assumed pattern speeds for the nuclear bar (400) and outer oval (45). The formal errors on $\Omega \pm \kappa/2$ become too large beyond 1 kpc to plot.

Figure 9 is a "resonance diagram" showing $\Omega(r) = v_{\rm rot}/r$, $\Omega - \kappa/2$, and $\Omega + \kappa/2$ as a function of radius. Here $\kappa$ is the epicyclic frequency, defined as

$$\kappa = \sqrt{\frac{2v}{r}\left(\frac{dv}{dr} + \frac{v}{r}\right)}.$$

The larger error bars in the H I rotation curve resulted in a poorer determination of $\Omega \pm \kappa/2$ at large radii, both because $\Omega$ is smaller and because $\kappa$ depends on the slope of the rotation curve. The data are clearly consistent with the proposal by Gerin et al. (1991) that the inner and outer rings (vertical dotted lines) correspond to the ILR
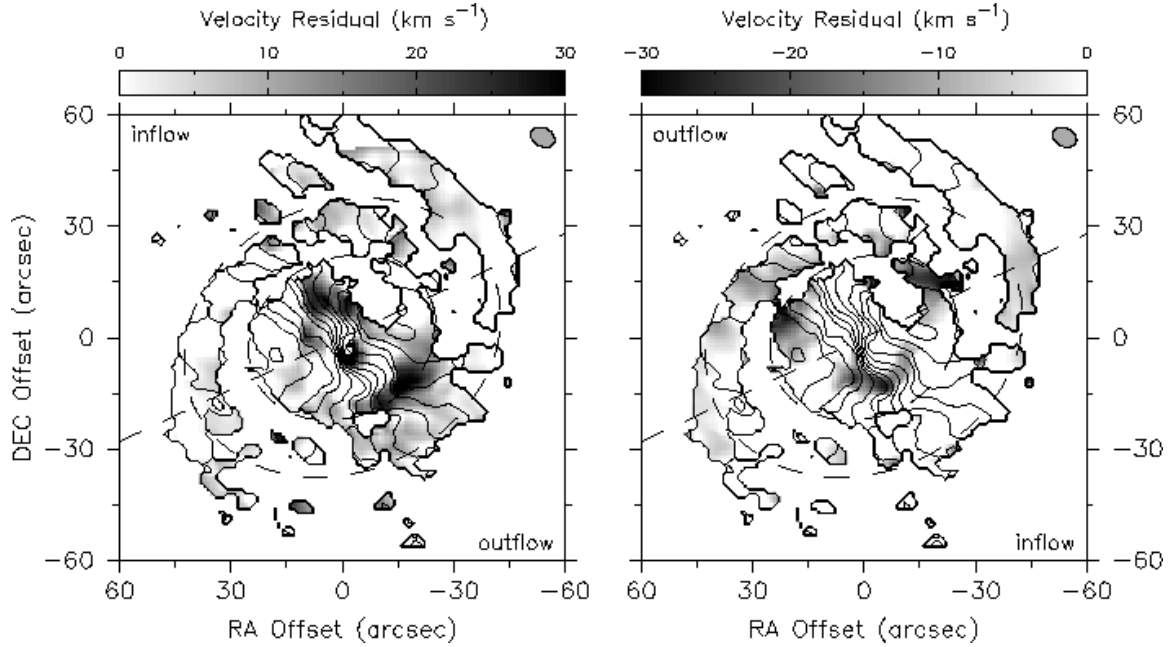
FIG. 10.— Velocity residuals $V_r(obs) - V_r(model)$, for the CO velocity field (shown in contours). Positive residuals are shown on the left and negative on the right; their interpretation as inflow or outflow are shown in the plot corners. The assumed line of nodes (galaxy major axis) is shown as a dashed line, and the dashed ellipses at $26''$ and $44''$ are the CR and OLR of the kinematic model discussed in the text.
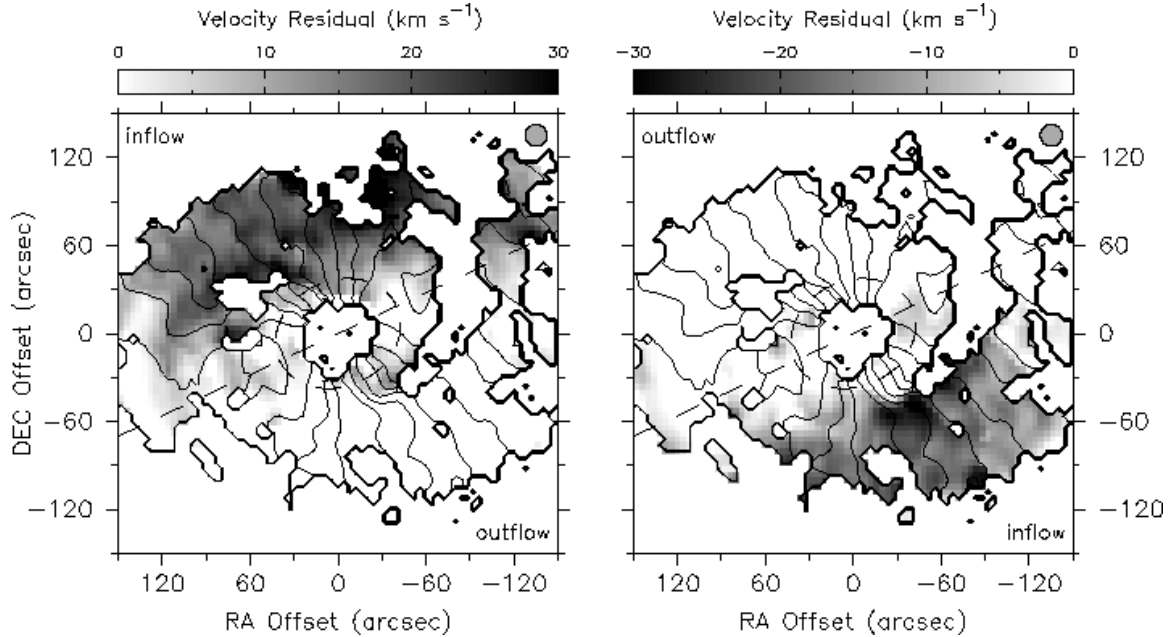


FIG. 11.— Velocity residuals $V_r(obs) - V_r(model)$, for the H I velocity field (shown in contours). Positive residuals are shown on the left and negative on the right; their interpretation as inflow or outflow are shown in the plot corners. The assumed line of nodes is shown as a dashed line, and a dashed ellipse at $r=44''$ is shown for comparison with Figure 10.

$(\Omega_p = \Omega - \kappa/2)$ and OLR $(\Omega_p = \Omega + \kappa/2)$ of an oval distortion with pattern speed $\Omega_p = 45$ km s$^{-1}$ kpc$^{-1}$, but the uncertainties are large. Further kinematic evidence in support of this interpretation is given in §4.4. At smaller radii, the CO data confirm that if the inner ring corresponds to the OLR of the nuclear bar, as suggested by MMG95, then the CR is located at $r \approx 26''$, just beyond the end of the nuclear bar (the bar ends at $r \approx 20''$ if deprojected). A corresponding pattern speed of 400 km s$^{-1}$ kpc$^{-1}$ is plotted, equivalent to the pattern speed of 290 km s$^{-1}$ kpc$^{-1}$ derived by MMG95 if scaled to their adopted distance (6.6 Mpc). We discuss the justification for these pattern speeds in §6.2.

## 4.2. Velocity Residuals

The adopted rotation curve was used to generate a model velocity field, in which the position angle of the line of nodes (defined as the line formed by the intersection of the galaxy plane with the "plane" of the sky) was fixed at 295°, the average value of $\phi_{kin}$ for the inner disk. The model field was then subtracted from the observed velocity fields to generate maps of residual velocities. Assuming the spiral arms are trailing, we infer that the near side of the galaxy is the northern side. Thus, if interpreted as motions in the galaxy plane, positive velocity residuals on the northern half of the galaxy's minor axis indicate a *radially inward* velocity component (i.e. local inflow), while they correspond to local outflow on the southern half. The CO and H I residual velocity maps are shown in Figures 10 and 11 respectively. The uncertainty in the mean line-of-sight velocity from the Gaussian fits is typically less than 5 km s$^{-1}$, increasing to ∼10 km s$^{-1}$ in regions with poor signal-to-noise or in the circumnuclear region where line profiles are broad.

The CO velocity residuals in the vicinity of the molecular bar ($r < 40''$) reveal strong non-circular motions, regardless of the choice of PA. As expected, the residuals are largest near the minor axis (25–30 km s$^{-1}$), since points near the major axis are weighted more heavily in determining the rotation curve. The sign of the residuals corresponds to local inflow near the ends of the nuclear bar and outflow between the southern end of the bar and the ring. However, these large flow velocities (40–50 km s$^{-1}$ in the plane of the galaxy) need not correspond to *net* radial flows if we are viewing elliptical orbits in projection. This indeed appears to be the case, as discussed in §4.6.

The residuals are generally <10 km s$^{-1}$ in the vicinity of the ring ($r=40''$–$50''$), where both the H I and CO velocity fields are well-described by pure circular rotation. This is somewhat surprising given that van der Kruit (1976) and Buta (1988) found clear evidence for an asymmetry in the Hα velocity field at the ring, with "a steep linear rise in the velocity across the ring on the southeast side" (Buta 1988). The ionized gas may possess small-scale velocity structure due to recent star formation to which the neutral gas is less sensitive. Furthermore, the interpretation by van der Kruit (1976) of the ring as an expanding feature was based on an assumed line-of-nodes position angle of 302°. In this paper we have adopted a PA of 295°, which eliminates the outflow signature at the ring at the expense of producing an inflow signature outside the ring.

Indeed, as shown in Figure 11, the H I velocity residuals

become large ($\gtrsim$20 km s$^{-1}$) outside the ring, showing a clear dipole pattern indicative of inward motion on both sides of the major axis. While this pattern is characteristic of radial inflow (van der Kruit & Allen 1978), it can also be interpreted as an error in $\phi_{kin}$. In Figure 12 we show the results of allowing the PA to vary with radius in the tilted-ring fit. An increase in $\phi_{kin}$ by about 15° between $r=50''$ and $100''$ is sufficient to remove most of the dipole signature and leave only isolated residuals, typically <10 km s$^{-1}$. Note that the isophotal PA also exhibits a variation with radius, but in the *opposite* direction, a point which we return to in §4.5 and §4.6.
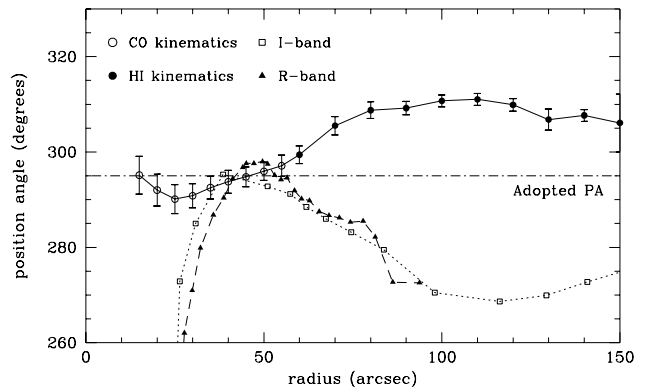


FIG. 12.— Major axis position angle (defined from 180°–360°) as a function of radius, derived from isophotal data as well as from CO and H I kinematics. The *I*-band data is from MMG95 and the *R*-band data is from Mulder (1995).

## 4.3. Position-Velocity Diagrams

Since two-dimensional velocity fields are insensitive to the presence of multiple velocity components or changes in spectral line profiles, we constructed position-velocity (p-v) maps for slices at various angles through the CO and H I datacubes. Figure 13 shows a slice through the CO cube along the nuclear bar (PA=28°). This slice is close to the kinematic minor axis (PA=25°), so the predicted velocities from the fitted circular rotation model are close to $V_{sys}$=315 km s$^{-1}$, as shown by the heavy solid line. The actual CO emission, however, departs strongly from this model. Part of the discrepancy is due to beam smearing of the galaxy's rotation, which is especially severe in the central regions of the galaxy where the velocity gradient is large. This will increase the velocity extent of the emission in the p-v diagram, and contributes to the large linewidths in the region from $-5''$ to $+5''$ (delimited by the dashed lines). In addition, however, there are regions where the CO emission is offset in velocity by $\gtrsim$20 km s$^{-1}$ from the circular rotation model. These include the regions labeled X in Figure 13, which occur at the ends of the bar where the local gas velocities are *inward*, as indicated by the negative velocity offset on the southwest side and the positive offset on the northeast side (cf. Figure 10). Similarly, the region labeled Y represents local *outward* velocities between the bar and the ring. The presence of these features in the p-v diagram confirms our earlier deductions from the velocity residual maps (§4.2).
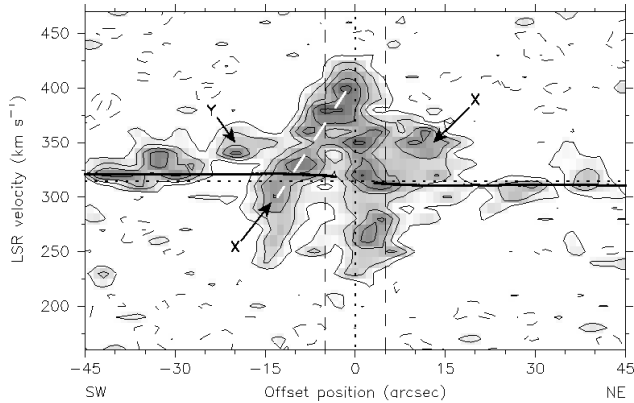
FIG. 13.— Position-velocity map of CO emission along a cut having a position angle of 28° (parallel to the nuclear bar) and passing through the galaxy center. Contour levels are $\pm\sigma\ldots\pm6\sigma$, where $\sigma$=70 mJy bm$^{-1}$. Dotted horizontal and vertical lines correspond to the systemic velocity and galaxy center. Dashed vertical lines at $\pm5''$ delineate the circumnuclear region where beam smearing of the galaxy's rotation may dominate. Regions of local inflow and outflow are labeled X and Y respectively. The thick solid line is the velocity curve predicted by the fitted rotation model.

The large velocity difference between regions X and Y on the southern side of the bar may indicate that the streaming motions associated with the bar (region X) are different from those in the spiral arm close to the bar end (region Y). Such a change in the direction of radial streaming motions is expected when crossing a bar's corotation radius (Combes 1988). Using our assumed pattern speed (§4.1), the CR occurs at an offset position of $21''$ along this slice. Also apparent in Figure 13 is a transition from locally inward to outward gas motion in going from region X on the SW side ($-15''$) towards the center (along the white dashed line). Since the inward velocity component at X is well-modeled by gas moving in elliptical streamlines (§4.6), the transition to radially outward motion may indicate a change in the orientation of the elliptical gas orbits. Higher resolution data would be valuable in exploring this possibility.
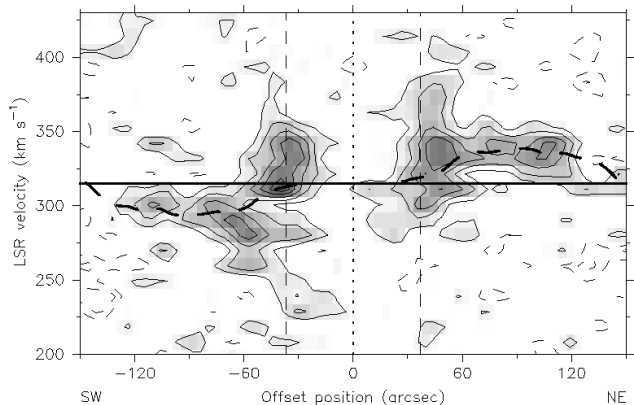


FIG. 14.— Position-velocity map of H I emission, binned to a velocity resolution of 10.4 km s$^{-1}$, along the assumed minor axis (PA=25°). Contour levels are $\pm\sigma\ldots\pm6\sigma$, where $\sigma$=1.5 mJy bm$^{-1}$. The thick solid line is the systemic velocity, which should be the centroid of the emission according to the disk model with PA fixed. The thick dashed line is the velocity curve predicted if the PA is allowed to vary with radius (cf. Figure 12). The dashed vertical lines mark the location of the H$\alpha$ ring.

Figure 14 displays a p-v slice through the H I cube along the assumed minor axis (PA=25°). While the circular rotation model predicts that the emission will be centered at $V_{\rm sys}$ (heavy solid line), the H I emission deviates quite strongly from this model, displaying the inflow signature that was already noted in the velocity residuals (§4.2). On the southwestern side, there is a striking transition from positive to negative velocity residuals as one crosses the ring (vertical dashed line), corresponding to relative outflow on the inner side of the ring (where the CO also shows outflow) and inflow on the outer side. Precisely such a signature is expected when crossing a Lindblad resonance, as discussed in §6.2. The heavy dashed line represents a best-fit model in which the PA is allowed to vary with radius, as in Figure 12. Note that even this model does not completely account for the velocity offsets at around $\pm60''$.

We conclude that while the p-v diagrams allow for a more detailed view of the kinematics in certain regions, they are generally consistent with the non-circular motions inferred from the velocity residual maps.

### 4.4. Radial Inflow Model

In the following sections we explore three physical models which may account for the non-circular motions seen in the velocity residuals and p-v diagrams. The first model we consider has gas moving in circular coplanar orbits superposed on a component of uniform radial contraction or expansion. In the ROTCUR program it is possible to fix the disk parameters and fit simultaneously for rotation and expansion velocities:

$$V(x,y) = V_{\rm sys} + v_{\rm rot}(r)\sin i\cos\theta + v_{\rm exp}(r)\sin i\sin\theta . \quad (2)$$

The resulting inflow velocities ($v_{\rm in} = -v_{\rm exp}$) are shown in Figure 15a. The inclusion of this additional velocity term virtually eliminates the dipole signature seen in Figure 11, since the effect of axisymmetric inflow on the velocity field of a galaxy is almost indistinguishable from an error in $\phi_{kin}$, at least for a nearly face-on galaxy such as NGC 4736. In the presence of radial inflow, the kinematic major axis ($\phi_{kin}$) rotates by an angle defined by

$$\tan\Delta\phi_{kin} = \alpha\cos i ,$$

where $i$ is the inclination from face-on and $\alpha$ is the ratio of the inflow speed to the circular speed, while the kinematic minor axis (systemic velocity contour) rotates by a somewhat larger angle:

$$\tan\Delta\phi_{min} = \alpha/(\cos i) .$$

Note that for a more highly inclined galaxy, it would be easier to distinguish inflow from an error in $\phi_{kin}$ because inflow would lead to a change in $\phi_{min}$ different from that in $\phi_{kin}$.

The zero point for $v_{\rm in}$ in Figure 15a is quite sensitive to the assumed value of $\phi_{kin}$: each 5° increase in the adopted $\phi_{kin}$ is equivalent to roughly a 15 km s$^{-1}$ decrease in $v_{\rm in}$ at all radii. Since the isophotal position angle decreases from about 295° to 270° between $45''$–$100''$, there appears to be a great deal of freedom in setting this zero point (although adopting a smaller $\phi_{kin}$ would only *increase* the inflow velocity). Under the assumption that the galaxy is not warped in these regions, we still consider 295° the most likely value for the true line-of-nodes PA, because outside the ring the kinematic and isophotal position angles disagree, but both are consistent with $\phi$=295° at the

ring (Figure 12). This choice also agrees with theoretical expectations in the context of an inflow model: (1) it causes the inflow velocity at the radius of the ring to vanish, with outflow interior to the ring and inflow exterior to it, conditions which seem appropriate for the formation of a gaseous ring; (2) the resulting sign changes in $v_{in}$ occur at the probable resonances of the oval distortion: a transition from outflow to inflow at $r \approx 45''$ (ILR) and from inflow to outflow at $r \approx 200''$ (CR), consistent with the predicted torques exerted on gas by a bar (Combes 1988; Schwarz 1981); (3) there is no significant $v_{in}$ outside the OLR of the oval ($r \approx 330''$), as expected from its reduced gravitational influence.



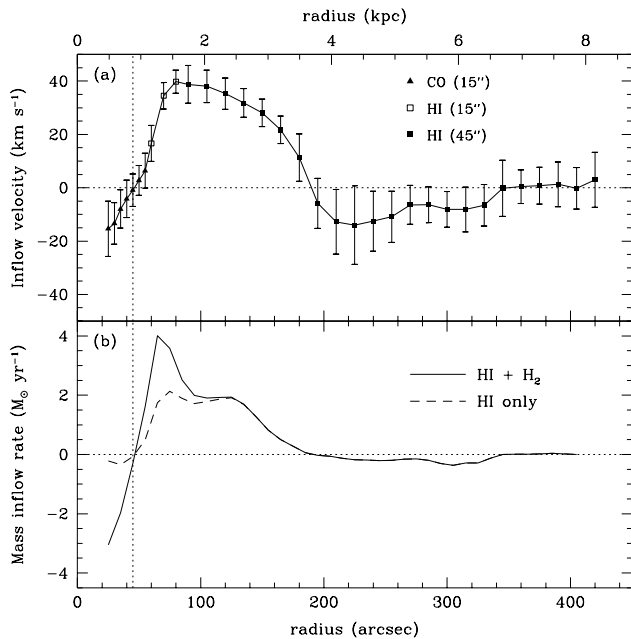FIG. 15.— (a) Fitted inflow velocity ($v_{in} = -v_{exp}$) as a function of radius, with disk parameters fixed at $\phi = 295°$, $i = 35°$. The curve is based on the same datasets used for Figure 8. (b) Inferred mass inflow rate as a function of radius, based on panel (a) and the 15″ resolution gas profiles. The vertical dotted line represents the location of the inner ring.

Figure 15b shows the inferred mass accretion rate as a function of radius,

$$\dot{M}(r) = 2\pi r \Sigma_{gas} v_{in} .$$

If the molecular gas is assumed to participate in the same radial inflow as the atomic gas, the mass inflow rate reaches a maximum of 4 M$_\odot$ yr$^{-1}$ at $r=65''$. However, the validity of this assumption is unclear due to the lack of CO detected outside the ring. Considering only the atomic gas, an inflow rate of $\sim$2 M$_\odot$ yr$^{-1}$ is implied. This is within a factor of 2 of the estimates given by Regan et al. (1997) for NGC 1530 ($1^{+2}_{-0.5}$ M$_\odot$ yr$^{-1}$) and Quillen et al. (1995) for NGC 7479 ($4\pm2$ M$_\odot$ yr$^{-1}$), both strongly barred galaxies. In neither of these cases, however, was the inflow assumed to be axisymmetric. For comparison, the rate at which gas is consumed by star formation in the ring is approximately 0.2 M$_\odot$ yr$^{-1}$ (§6.6).

The most disturbing aspect of a pure inflow model is the high (up to 40 km s$^{-1}$) inflow velocities required to explain the residuals outside the ring. These speeds are

well above the likely sound speed and would therefore create strong shocks. Of course, such shocks are precisely what is needed to drive rapid inflows in the first place, but one would expect them to be confined to localized regions, e.g. where the gas first encounters a spiral arm (Roberts 1969; Shu, Milione, & Roberts 1973), contrary to what is seen in Figure 11. Another problem is the relatively short timescale on which the H I outside the ring would flow inward. The mass-weighted mean flow velocity in the annulus from $r=80''$–$190''$—where the radial flow is inward and where most of the H I outside the ring lies—would be 32 km s$^{-1}$, sufficient to clear out that region in $\sim$70 Myr. This timescale is much shorter than the Hubble time or the gas consumption timescale (§5.2) and indeed is comparable to the orbital (dynamical) timescale.

Our analysis highlights the intrinsic difficulty in measuring *subsonic* inflow speeds in galaxy disks. For a moderately inclined galaxy, detection of a 5 km s$^{-1}$ inflow velocity against a circular speed of $\sim$200 km s$^{-1}$ requires being able to determine a shift in the kinematic position angle of $\sim$1°. Large inclination angles ($i > 55°$) would be necessary to create a shift of several degrees in the kinematic minor axis, but then beam-smearing effects and the finite thickness of the disk complicate the interpretation.

### 4.5. *Warped Disk Model*

The increase in kinematic position angle with radius, in the region outside the ring, may be an indication of a warp in the disk—in other words, the gas orbits may not be coplanar. Warps in the stellar disk are generally not seen well inside the optical radius of a galaxy (Kormendy 1982); on the other hand, a strong ($\sim$25°) tilt in the molecular and atomic gas layer has been inferred for the inner 2 kpc of our Galaxy (Burton & Liszt 1978; Liszt & Burton 1980), suggesting that the gas disk can deviate substantially from the midplane of the galaxy. The classic signature of a warp is a progressive variation in the values of both $i$ and $\phi$ produced by a tilted-ring fit, usually occurring beyond a certain radius. Unfortunately, we find that allowing both parameters to vary with radius results in a poor fit unless the rotation velocities were also fixed, another indication of the tight coupling between $v_{rot}$ and $i$. Hence the data do not allow a clear determination of how $i$ may change with radius.

The most serious objection to a warp model is that while there does seem to be a connection between the change in optical morphology and the change in kinematics outside the ring, they cannot both be explained by a warp, since the isophotal PA decreases as the kinematic PA increases (Figure 12). For a warped disk one expects the two angles to change in the same direction. Furthermore, since the change in $\phi_{kin}$ reverses itself at larger radii (cf. Figure 15a), the direction of the warp would also have to reverse direction.

### 4.6. *Elliptical Streaming Model*

The divergence of the isophotal and kinematic position angles shown in Figure 12 is best explained as an effect of elliptical orbits when seen in projection. This is because the kinematic major axis is defined as the locus of maximum line-of-sight velocity, which for elliptical orbits will generally *not* occur when a parcel of gas is at its largest

distance from the galaxy's center (apogalacticon)—which in turn may not even coincide with the major axis of the ellipse as viewed in the sky! To illustrate this property, we used the NEMO software package (Teuben 1995) to generate a simple model of oval orbits by stretching circular orbits by $\epsilon^{1/2}$ and $\epsilon^{-1/2}$ along the $x$ and $y$ axes respectively and scaling the circular velocities by $\epsilon^{-1}$ and $\epsilon$, the correct scaling for a harmonic potential ($\kappa = 2\Omega$). A value of $\epsilon=1.2$ was used, based on the ellipticity of the oval distortion in NGC 4736, and the orbits were rotated and inclined to the line of sight so that they appeared as ellipses with a position angle of $-27°$ relative to the true line of nodes—this value should approximate the isophotal PA if the orbits are aligned with a barred potential. The resulting *kinematic* position angle as a function of radius is shown by the solid line in Figure 16(c). Due to projection effects, the true line of nodes ($\phi=0°$) has a PA greater than the isophotal PA ($\phi=-27°$, not shown) but less than the kinematic PA ($\phi=5°–10°$), similar to what is seen in the NGC 4736 data (Figure 12).
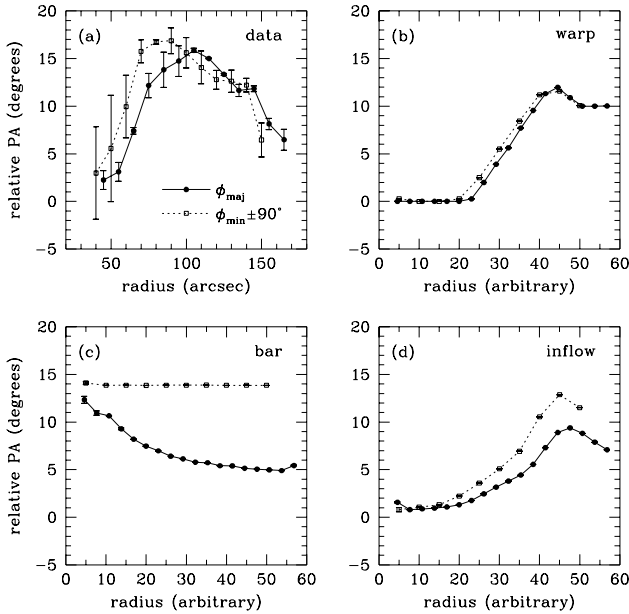


Fig. 16.— Position angles of the kinematic major and minor axes as a function of radius for the H I data and three kinematic models (warped disk, elliptical orbits aligned with a bar, and radial inflow). For each axis the PA has been determined independently on each side of the galaxy center; the plotted points are the average values and the error bars represent the difference between the two measurements. The assumed line of nodes is taken to be 0°.

Figure 16 also reveals another characteristic of this simple bar model, namely that the kinematic major and minor axes do not remain perpendicular—a property that is commonly observed in barred galaxies (Bosma 1978). For aligned elliptical orbits, the minor axis is expected to remain constant with radius, while the major axis drifts away from it. Yet for NGC 4736, the H I data outside the ring (Figure 16a) show that the two axes stay approximately perpendicular even as they drift by $10°–15°$. In this respect, the data agree better with the warp and inflow models discussed above and shown schematically in panels (b) and (d).

Elliptical streaming should also produce distinctive sig-

natures in the velocity residuals as a function of $\theta$ (the angle in galactic plane), as discussed by Teuben (1991). In the simplest approximation, the requirement of no net inflow suggests that the expansion velocity in Equation 2 (§4.4) takes the form

$$v_{\exp} \propto \sin 2(\theta + \theta_0)$$

where $\theta_0$ is a phase shift dependent on the orientation of the orbits. In other words, the expansion velocity is positive in two quadrants and negative in the other two. In the special case where we view the orbits end-on or edge-on ($\theta_0=0°$ or $90°$), the velocity residuals have a $\cos 3\theta$ form (cf. Equations 1 & 2), and the oval orbits mimic circular orbits with a different value for the disk inclination (van der Kruit & Allen 1978). In the more general case where the bar has some arbitrary angle to the line of nodes, the residuals will be dominated by a linear combination of $\sin \theta$ and $\cos(3\theta + 2\theta_0)$, with the $\cos 3\theta$ wave being the stronger of the two. Then the velocity field *cannot* be modeled in terms of circular orbits, since one can remove the $\sin \theta$ term with an appropriate choice of $\phi_{kin}$, but attributing the remaining $\cos 3\theta$ term to inclination would have required a different $\phi_{kin}$ due to the phase shift $\theta_0$.
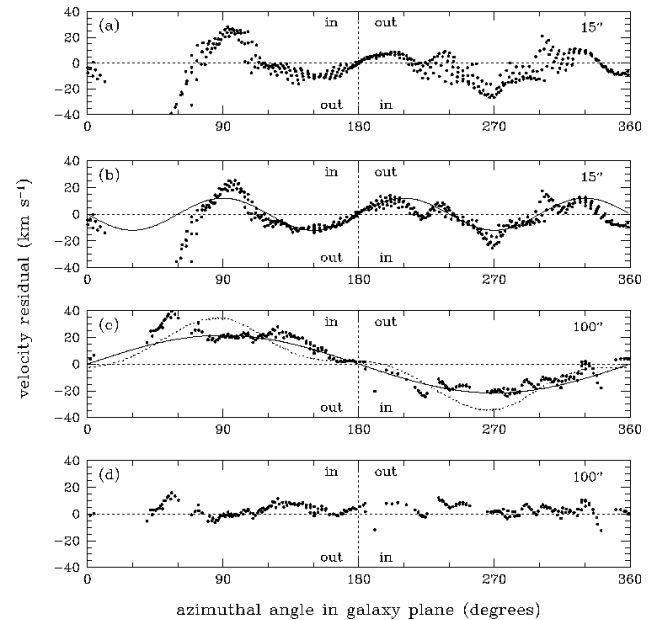


Fig. 17.— Velocity residuals plotted in galactocentric rings. Panels (a) and (b) show the CO residuals at $r=15''–20''$ before and after fitting a $\sin \theta$ (varying PA) component. A $\sin 3\theta$ curve is shown in panel (b). Panels (c) and (d) show the same analysis for the H I residuals at $r=100''–110''$. The solid line in panel (c) approximates the best-fit $\sin \theta$ curve, while the dotted line is a prediction for an elliptical streaming model. Residuals correspond to the directions of inflow and outflow as marked. See text for discussion.

These simple predictions for elliptical streaming agree qualitatively with the kinematics in the inner CO disk. As Figure 17 shows, in the annulus from $r=15''–20''$ there is a clear $\sin 3\theta$ term in the residuals. This persists in roughly the same form even after removal of a $\sin \theta$ term (i.e. freely varying PA) in panel (b). The curve drawn has the form $V_{res} = -12 \sin 3\theta$ km s$^{-1}$ and is a reasonably good fit to the data. We conclude that the velocity residuals in this region are due primarily to elliptical streaming in the bar potential. In light of the preceding discussion,

the presence of a $\sin 3\theta$ rather than $\cos 3\theta$ residual suggests that the major axis of the orbits would be oriented $\sim 45°$ away from the line of nodes if the galaxy were viewed face-on. While this is somewhat puzzling since we appear to be looking at the bar close to end-on, we do not expect our rough analysis to yield exact agreement with the data (for instance, we have neglected the $\theta$ dependence of $v_{\rm rot}$ in Eq. 2).

In contrast, the H I residuals outside the ring are dominated by a $\sin\theta$ term (Figure 17c), which upon removal reveals little if any $\cos 3\theta$ component (Figure 17d). This is inconsistent with gas streaming in aligned elliptical orbits, in which case one would expect the strong $\cos 3\theta$ term to produce residuals with a more cusped appearance (dotted line in Figure 17c). Rather, the dominance of the $\sin\theta$ (dipole) term agrees better with the radial inflow model. In §6.1 we discuss possible ways in which an elliptical streaming model could be made more consistent with the observations.

## 5. STAR FORMATION

### 5.1. *Determination of the SFR*

As noted by Kennicutt (1998b), $H\alpha$ is a sensitive tracer of the Lyman continuum flux, which is primarily due to stars with masses $>10$ $M_\odot$ and lifetimes $<20$ Myr. Ignoring extinction and adopting a Salpeter IMF, we convert the $H\alpha$ flux to an SFR using the formula (Kennicutt 1998b):

$$\frac{\rm SFR}{M_\odot\ {\rm yr}^{-1}} = 7.9 \times 10^{-42}\ \left(\frac{L_{\rm H\alpha}}{\rm erg\ s^{-1}}\right)\ .$$

Although uncertainties in the IMF and the escape fraction of ionizing photons can significantly affect the SFR, probably the largest source of uncertainty when comparing regions within a galaxy is variable extinction due to dust in the galaxy's disk. (For NGC 4736, extinction due to dust in our Galaxy is likely to be minimal at a Galactic latitude of 76°.) A rough estimate of the extinction at $H\alpha$ can be derived by assuming an extinction law of $N_H/A_V = 2 \times 10^{21}$ cm$^{-2}$ mag$^{-1}$ and $A_R/A_V = 0.75$ (Bohlin, Savage, & Drake 1978; Rieke & Lebofsky 1985). For NGC 4736, if the H II regions are located in the midplane, this scaling gives typical values of $A_R \sim 0.75$ at the ring ($r=45''$), $\sim 2.5$ in the molecular bar ($r=10$–$20''$), and $\sim 4$–$9$ at the nucleus ($r < 5''$). However, this assumes a constant gas-to-dust ratio across a huge range of environments as well as uniform mixing of dust. A better way to test the importance of extinction is to measure the thermal bremsstrahlung emitted in the radio, which is transparent to dust; the main difficulties are that synchrotron emission from supernova remnants is likely to dominate and good sensitivities are difficult to achieve. Still, the VLA observations of Turner & Ho (1994) and Duric & Dittmar (1988) appear to show very little thermal emission interior to the ring; Turner & Ho (1994) estimate a thermal flux of 2 mJy for the central $1' \times 1'$, compared to 13 mJy in the ring. These results are consistent with the non-detection of Br$\gamma$ emission from the nucleus by Walker et al. (1988). We conclude that while extinction is likely to be important in the nuclear region, infrared and radio observations show no indication that high levels of star formation are occurring there. On the other hand, there are spectroscopic indications of a young stellar population in the nucleus,

implying that the SFR in the nucleus was much higher $\sim 1$ Gyr ago (Pritchet 1977; Walker et al. 1988).

The $H\alpha$ image contains emission from the [N II] line as well. Spectroscopy by Smith et al. (1991) indicates that 62% of the emission in the ring is due to $H\alpha$, and this ratio has been used to correct the fluxes before conversion to star formation rates. In the nuclear region Smith et al. (1991) found that only 24% of the emission is due to $H\alpha$; given the large uncertainty in the $H\alpha$ flux from this region anyway, we have not bothered to apply a different correction.

### 5.2. *Gas Consumption Timescales*

The CO profile and the adopted SFR profile are shown in Figure 18, at $6''$ resolution. The ratio of the two profiles gives a nominal gas consumption time $\tau_{\rm gas} \equiv \Sigma_{\rm gas}/\Sigma_{\rm SFR}$. Due to the neglect of gas recycling by evolved stars, which may extend these times by factors of $\sim 2$ (Kennicutt, Tamblyn, & Congdon 1994), and uncertainties in the CO-to-H$_2$ and $H\alpha$-to-SFR conversions, these times should be considered very approximate. Nonetheless, it is clear that the gas consumption time within the ring ($\sim 1$ Gyr) is much less than a Hubble time, as one would expect in a starburst. We neglect the H I contribution to $\Sigma_{\rm gas}$, which is small ($\lesssim 25$%) in this region.
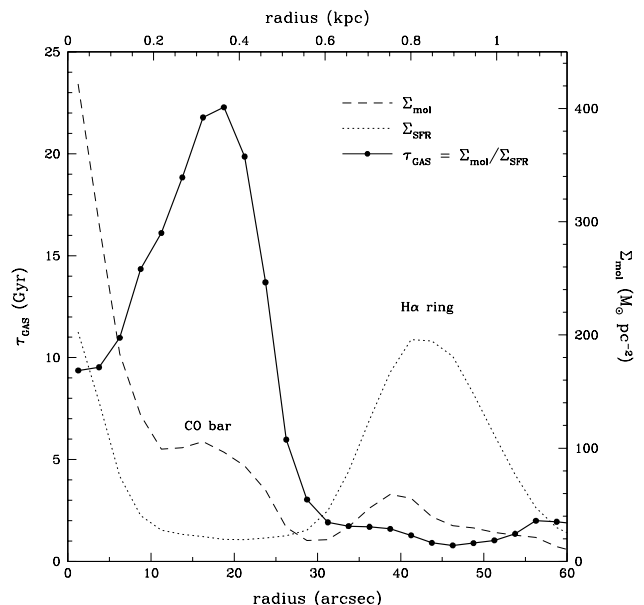


FIG. 18.— Radial profiles of CO (robustly weighted cube) and $H\alpha$, after conversion into molecular gas surface density and SFR surface density respectively, and their ratio, the gas consumption time.

Focusing now on the radial variation in $\tau_{\rm gas}$, the most striking trend is the very long gas consumption time in the vicinity of the molecular bar ($r=10''$–$30''$) in comparison with the ring. Equivalently, the star formation efficiency, as measured by $\Sigma_{\rm SFR}/\Sigma_{\rm gas} = \tau_{\rm gas}^{-1}$, is much higher in the ring than in the inner disk. (We define the SFE here as the star formation rate per unit gas mass, since the fraction of gas converted into stars is only well-defined for an individual cloud.) It is possible that some of this difference is due to dust extinction obscuring star formation near the nu-

cleus and a standard X-factor overestimating the amount of molecular gas. We discuss these possibilities further in §6.3.2.

Our interpretation of $\tau_{\rm gas}$ as the gas consumption time and $\tau_{\rm gas}^{-1}$ as the star formation efficiency assumes that $\Sigma_{\rm gas}$ and $\Sigma_{\rm SFR}$ are close to their time-averaged values. This will probably not be true on a point-by-point basis, due to evolutionary effects and a bias towards observing massive stars in regions which have been cleared of dense gas, but it may be approximately true when averaging azimuthally within rings. However, in regions where star formation on large scales is episodic (e.g., controlled by a threshold density), unusually high or low star formation efficiencies will be inferred depending on whether we are observing the galaxy in an active or quiescent star-forming phase.
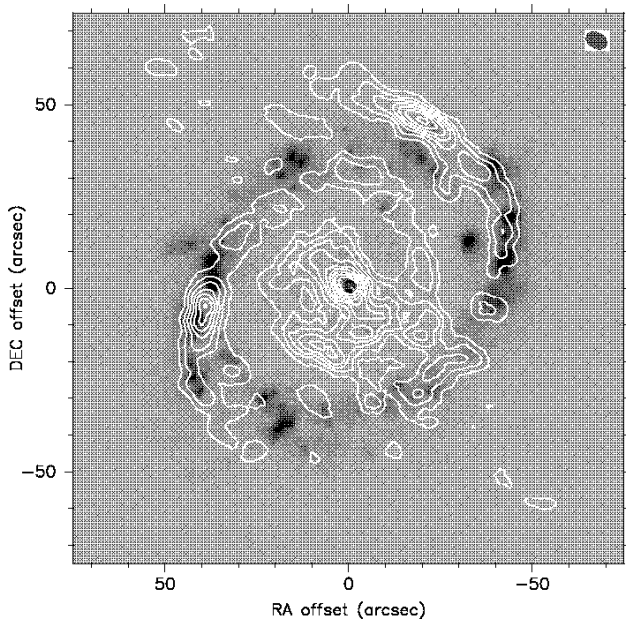
shift is only marginal.

There is no obvious explanation for the differences in these symmetries, although the symmetries themselves are likely to be mainfestations of density wave resonances—a clear indication that the star formation process is controlled in part by the global dynamics of the galaxy. The presence of twofold symmetry in both H I and Hα distributions is consistent with the earlier suggestion (§3.1) that H I is mainly a photodissociation product, but Figure 20 also shows that the detailed correspondence between Hα and H I is poor. We examine this issue further in §6.4. The presence of a threefold symmetry in the CO distribution may result from an interaction of underlying $m=1$ and $m=2$ modes, as has been suggested by Elmegreen, Elmegreen, & Montenegro (1992) from studies of other spiral galaxies.
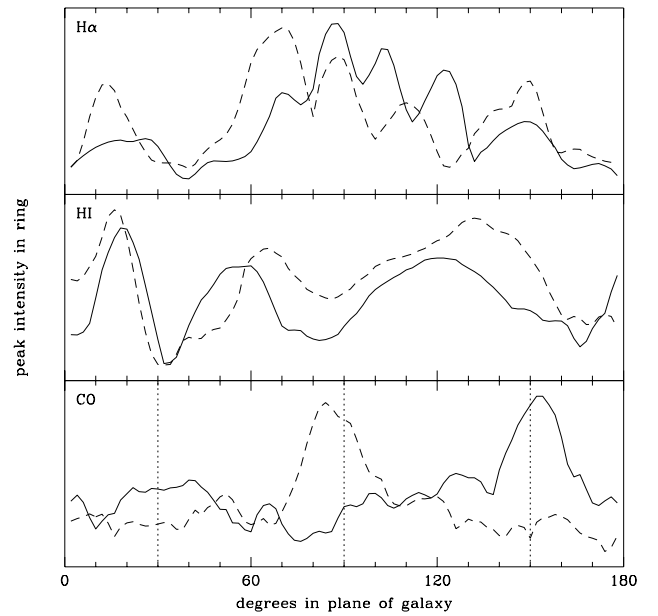


FIG. 19.— CO contours as in Figure 4 overlaid on the Hα image of Pogge (1989).



FIG. 20.— Azimuthal profiles of Hα, H I, and CO peak intensity in the ring ($r=30$–$60''$). The azimuthal angle increases counter-clockwise from due south (PA=180°). The dashed lines are the continuation of the profile on the other side of the galaxy. The dotted lines in the bottom panel are spaced by 120° and highlight the threefold symmetry of the CO.

### 5.3. *Azimuthal Symmetry*

A feature that is not apparent in the radial profiles is the remarkable 180° rotational symmetry in the Hα ring (Figure 19), in stark contrast to the distribution of CO emission. This is truly unexpected if, as we expect, star formation is associated with molecular clouds. We compare the symmetry properties of the Hα, and H I, and CO in Figure 20, which shows the peak intensity in the ring as a function of azimuth from an arbitrarily chosen reference point. The Hα and H I show a good twofold symmetry (dashed and solid lines agree well, with a linear correlation coefficient of 0.4–0.5) while the CO distribution shows poor twofold symmetry (linear correlation coefficient of $-0.4$). Instead, the CO distribution suggests a threefold symmetry as remarked on in §3.1, although the peak at 30° azimuth is weaker than the other two. A cross-correlation analysis shows that the H I and Hα distributions match best if we assume that the H I is shifted $\sim 45°$ upstream of the Hα (i.e. to the right in Figure 20). This corresponds to a time lag of 3.5 Myr using the adopted rotation curve, but the improvement in the correlation after making this

### 5.4. *Toomre Stability Criterion*

Can the radial variation in star formation efficiency be explained in terms of a simple gravitational stability analysis? In Figure 21 the SFR profile is plotted along with the ratio $Q$ of the critical density for gravitational instability, $\Sigma_{\rm crit} \equiv \kappa\sigma_v/\pi G$, to the gas surface density $\Sigma_{\rm gas}$. Thus, a value of $Q < 1$ corresponds to instability (Safranov 1960; Toomre 1964). This formula is strictly appropriate for axisymmetric (ring-like) perturbations only, and we discuss some of the caveats in the interpretation of $Q$ in §6.5. For the velocity dispersion $\sigma_v$ we have taken a value of 7 km s$^{-1}$ as determined from the Gaussian fits to the robust CO datacube where the major axis intersects the ring. This is compatible with the value of 6 km s$^{-1}$ assumed by Kennicutt (1989) as well as observations of H I in face-on galaxies (e.g. van der Kruit & Shostak 1984). Although beam smearing will lead to broadening of the CO line pro-

files by the galaxy's rotation, this effect is minimized near the major axis once the rotation curve has flattened. For a 6″ beam located 45″ from the center, which subtends an angle of ∼10° as measured in the plane of the galaxy, the azimuthal velocity gradient across the beam is negligible (<1 km s$^{-1}$) and the radial gradient is ∼4 km s$^{-1}$, based on the CO rotation curve. Correcting for this would only bring $\sigma_v$ down to 6 km s$^{-1}$, and would be excessive since the edges of the beam actually carry less weight in the smearing. We also neglect the likely rise in velocity dispersion towards the galaxy center, but note that it would lead to a sharper rise in $Q$ than that shown in Figure 21.
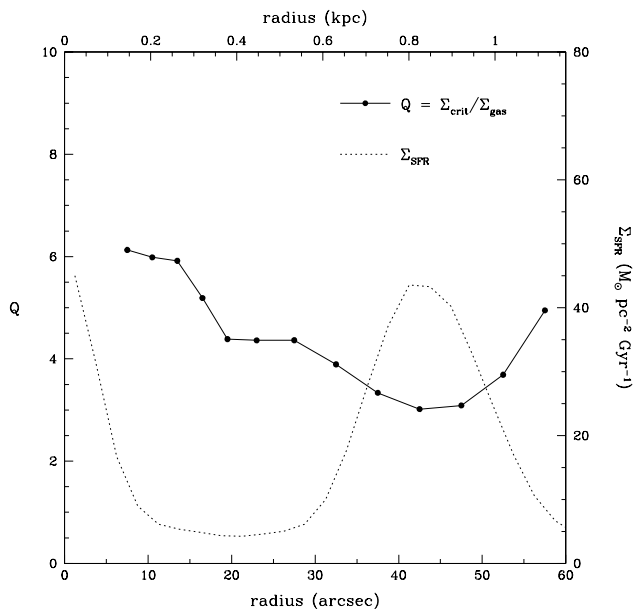


FIG. 21.— Radial profile of the Toomre $Q$ parameter (defined in text) superposed on the SFR profile.

The resulting $Q$ profile shows a clear minimum in the vicinity of the star-forming ring, consistent with a general picture in which star formation in the ring is triggered by gravitational instability. However, even here the *azimuthally averaged* gas density is a factor of ∼3 less than the critical density. As evident from the moment-0 map (Figure 4), the ring contains a number of molecular condensations which locally have surface densities (averaged over a ∼100-pc wide beam and corrected to face-on) of up to 300 M$_\odot$ pc$^{-2}$, somewhat higher than the critical density (∼200 M$_\odot$ pc$^{-2}$). Thus it may be possible for star formation to result from gravitational instability where *local* enhancements in the gas density occur, although a different process (e.g., non-axisymmetric instabilities) would be necessary to create these enhancements. The large value of $Q$ in the ring is discussed further in §6.5.

### 5.5. *The SFR–Gas Density Relationship*

As noted in §1, Kennicutt (1989, 1998a) has found that the disk-averaged SFR is much better correlated with the average H I density than with the average H$_2$ density. This result is independent of whether H$\alpha$, UV continuum, or far-infrared fluxes are used to derive the SFR, and is especially noticeable in low-luminosity galaxies, leading Kennicutt (1998a) to attribute it to the metallicity dependence

of the X-factor. He also finds that above the critical density, the relation between the SFR and *total* gas density is well-described by a Schmidt law, $\Sigma_{\rm SFR} \propto \Sigma_{\rm gas}^N$, with $N \sim$ 1.3–1.5. To investigate how well these conclusions apply within the disk of NGC 4736, we compared the fluxes of the three tracers CO, H$\alpha$, and H I when averaged in rings and on a point-by-point basis.
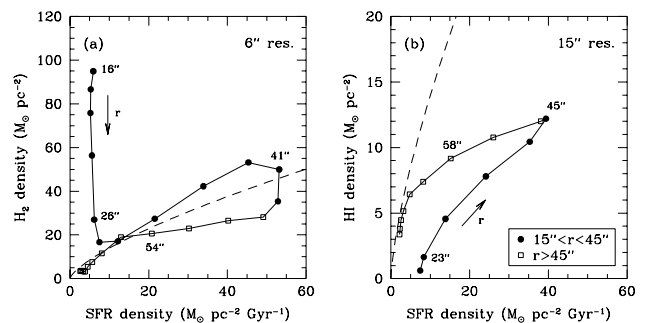


FIG. 22.— Comparison of SFR density with gas density, averaged in rings, for (a) CO data at 6″ resolution, (b) H I data at 15″ resolution. The CO data points begin at 16″ and are spaced by 2″.5; the H I data points start at 17″.5 and are spaced by 5″. The dashed line is the composite Schmidt law as given by Kennicutt (1998a).

Figure 22 shows this comparison for rings of constant width ranging from $r$=15″–75″ for the CO data and $r$=15″–90″ for the H I data. (We have excluded the nuclear region due to uncertainties in the H$\alpha$ flux there, §2.4 and §5.1.) The molecular gas (Figure 22a) dominates the gas density over most of this range in radius, and is thus most appropriate for comparing the SFR and total gas densities. The overall correlation between CO and H$\alpha$ is poor, since the distribution of points in the figure is strongly bimodal, with strong CO fluxes in the inner disk ($r < 30″$) where little star formation is occurring, in addition to the expected correlation in the vicinity of the ring ($r \approx 45″$). The dashed line is the composite Schmidt law given by Kennicutt (1998a),

$$\Sigma_{\rm SFR} = 0.25 \left( \frac{\Sigma_{\rm gas}}{1\,{\rm M_\odot\,pc^{-2}}} \right)^{1.4} {\rm M_\odot\,Gyr^{-1}\,pc^{-2}} \ .$$

This parametrization is based on averages over the star-forming disks of 61 normal galaxies and the ∼1 kpc-size inner disks of 36 starbursts, and has been shown to apply across a wide range of scales and galaxy types. Both the power-law index and the normalization are a surprisingly good match to the CO data outside of the inner disk, with the predicted gas densities lying within a factor of ∼1.5 of their actual values. Thus, when azimuthally averaged, star formation *in the ring only* appears to follow a Schmidt law. Interior to the ring, star formation falls well below the Schmidt law prediction. This is in agreement with the low star formation efficiency for the central region found in §5.2, and is discussed further in §6.3.2.

The azimuthally averaged H I emission, being strongly peaked at the ring, shows a good correlation with H$\alpha$, especially at high densities (Figure 22b). However, the SFR density rises well above the Schmidt law prediction except at large radii ($r > 70″$), which is not surprising given that most of the gas in the inner region is molecular. The positive correlation between H$\alpha$ and H I emission within a

region where the gas is primarily molecular lends further support to the hypothesis that H I in the ring is mostly a dissociation product (see §6.4).
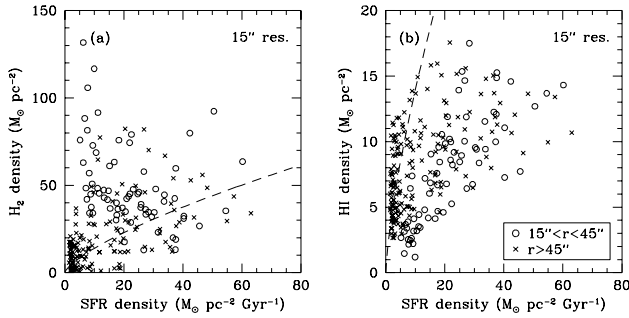


FIG. 23.— Comparison of SFR density with gas density, on a pixel-by-pixel basis, for (a) CO data, (b) H I data, both at 15″ resolution. Data have been output in 8″ pixels, so not all points are independent. The dashed line is the same as in Figure 22.

Since averaging in rings causes pixels in the galaxy center to be over-represented with respect to outer pixels, we also compared the images on a pixel-to-pixel basis (Figure 23). The overall trends noted above are confirmed: $\Sigma_{\rm SFR}$ is better correlated with $\Sigma_{\rm HI}$ (correlation coefficient 0.53) than with $\Sigma_{\rm H_2}$ (0.28), and $\Sigma_{\rm SFR}$ generally falls *below* the Schmidt Law prediction when only molecular gas is considered (particularly in the central regions) and *above* the prediction when only atomic gas in considered. On the other hand, there is a much larger scatter in the pixel-by-pixel comparison than in the azimuthal averages (Figure 22). Some amount of scatter will be introduced by measurement error (near zero flux) or pixellation effects, but mostly it is indicative of the small-scale anticorrelation between neutral and ionized gas that is apparent in Figure 19. This is largely an evolutionary effect (massive stars dissociate and ionize their natal clouds) and is greatly reduced by averaging in rings. Making sense of the additional information provided by *not* averaging in rings will require a more sophisticated analysis, to be pursued in a future study (Sheth et al., in preparation).

## 6. DISCUSSION

### 6.1. *Radial Inflow or Elliptical Streaming?*

Our analysis in §4 of inflow, warp, and elliptical streaming models indicates that no single model seems to account for all features of the data. The simultaneous variation of the kinematic and isophotal PA with radius, and the implied oval distortion in the stellar disk, point strongly towards elliptical streaming as the origin of the large-scale H I velocity residuals. On the other hand, the near-orthogonality of the major and minor axes and the azimuthal dependence of the velocity residuals disagrees with a simple model of gas flowing in aligned oval orbits and favors a radial inflow model, although the implied inflow speeds are large ($\sim$40 km s$^{-1}$). Elliptical streaming does seem to describe the residuals in the inner CO disk quite well, where the influence of the nuclear bar is strong. It may be that when applied to the weaker oval distortion, our elliptical streaming model is a poor description of reality.

In fact, oval gas orbits will not be aligned with the bar at

all radii because of the dissipative nature of the gas (Buta & Combes 1996). The principal orbits in a barred potential change orientations from parallel to perpendicular to the bar with each resonance crossing. The gas, however, cannot make this transition abruptly without collisions and dissipation, so it will tend to follow elliptical orbits that change orientation gradually with radius (Sanders & Huntley 1976). As shown in Figure 24, this will generate a spiral pattern in the gas due to orbit crowding, similar to what is actually observed in the H I (Figure 7). The velocity residuals also become more complicated in this situation. Although there should still be equal amounts of inflow and outflow across a circular ring, the crowding of orbits into spiral arms where the radial flow is inward (see Figure 24) leads to an observational bias against regions of outflow, where the gas surface density is low. This bias may contribute to the apparent inflow signature in NGC 4736, and since the direction of radial streaming motions along spiral arms changes across each resonance, it might also explain the reversals in $v_{\rm exp}$ shown in Figure 15. However, it appears doubtful whether sampling bias alone can account for the strong inflow signature just outside the ring, since the H I velocity field is well-sampled in azimuth in the region from $r$=40″–100″. Further work will therefore be needed to determine whether a model of misaligned oval orbits can reproduce the kinematics of this region.
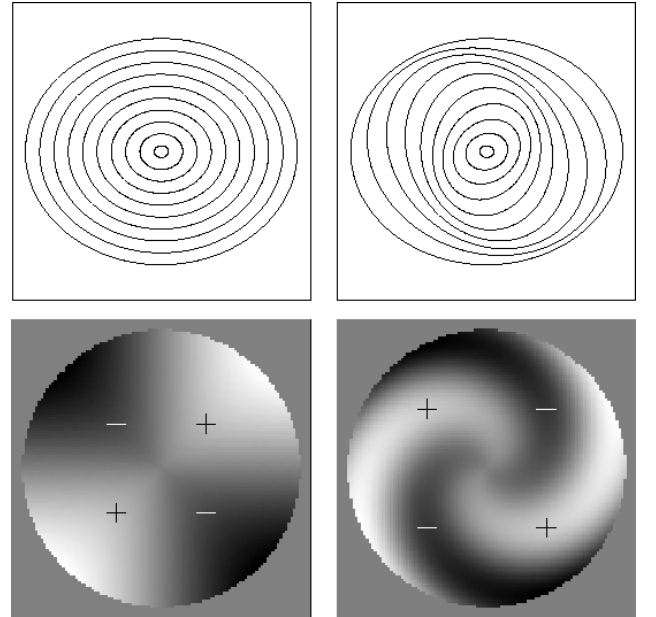


FIG. 24.— Orbit orientations (*top*) and radial expansion velocity (*bottom*) for two models: (*left*) aligned elliptical orbits; (*right*) orbits that have been precessed into a spiral pattern. The galaxy plane is viewed face-on, and velocities are measured in the disk plane, not along the line of sight. Note that for the aligned orbits, $v_{\rm exp} \propto \sin 2\theta$, whereas for the precessed orbits the locations of inflow and outflow form a spiral pattern. Both models assume a solid-body rotation curve and clockwise rotation.

An important point to note is that even if the H I residuals were due primarily to elliptical streaming in misaligned orbits, a small net inflow would still result from the torques exerted on the gas by the oval distortion in the potential (Combes 1988). Only orbits that are aligned parallel or

perpendicular to the oval experience no net torque; gas in misaligned orbits between ILR and CR is forced inward, while between CR and OLR it is forced outward. This gradual flow leads to mass accumulation at the ILR and OLR, but since the flow velocities required to form and sustain a ring are quite small (§6.6), they may only be observable in locations where strong shocks occur.

## 6.2. A Bar Within Oval System

The coexistence of a nuclear bar and large-scale oval distortion in NGC 4736 place it among a growing number of galaxies with multiple bars, as discussed by Friedli & Martinet (1993). These authors have conducted detailed simulations of the interaction and evolution of two bar structures rotating at different pattern speeds and concluded that significant radial mass transport can occur. Whether this scenario is applicable to a given galaxy, however, depends on the relative orientation of the two bars. While parallel or orthogonal nested bars can share the same pattern speed, for reasons of dynamical stability misaligned bars cannot do so (Louis & Gerhard 1988). Misaligned bars are therefore a good indication of different pattern speeds, although the intrinsic orientation of a bar structure is difficult to determine without prior knowledge of the inclination and position angle of the galaxy.

In the case of NGC 4736, the nuclear bar is oriented roughly along the kinematic minor axis of the galaxy, whereas the large-scale oval has a PA ($\sim$95°) that is 20°–25° less than the kinematic major axis (line of nodes), and will be even further away when deprojected with our assumed disk parameters (if the oval has an axis ratio of 0.75 as found by MMG95, its major axis will be 45° from the kinematic major axis when deprojected.) Thus the two bar structures in NGC 4736 appear to be neither aligned nor orthogonal, and we conclude that they are rotating at different pattern speeds, in agreement with MMG95.

Observational determination of the actual pattern speeds is difficult, and most methods have been designed for application to grand-design spiral galaxies (Buta & Combes 1996 and references therein). Our choice of pattern speeds places both the OLR of the central bar and the ILR of the oval distortion at the ring ($r \approx 45''$), consistent with previous studies (MMG95; Gerin et al. 1991). This scenario is supported by the following arguments:

1. Theoretical studies and modeling of observations suggest that bars end somewhat inside their corotation radius (Contopoulos et al. 1989; Athanassoula 1992; Laine, Shlosman, & Heller 1998). In NGC 4736 the nuclear bar extends out to $r_{bar} \approx 20''$ (deprojected), thus a corotation radius of $r=26''$ ($1.3\,r_{bar}$) is in agreement with this general rule.

2. For a flat rotation curve, the ratio of the OLR radius to the ILR radius is $(\sqrt{2}+1)/(\sqrt{2}-1) = 5.8$, roughly the ratio of the outer ring radius ($\sim$300'') to the inner ring radius ($\sim$50'').

3. As a result of changes in the orientation of the dominant stable orbits, the radial direction of spiral arm streaming motions and gravitational torques changes across each principal resonance (Combes 1988). Corresponding changes in the inflow velocity are seen in the data (Figure 15). Regardless of whether the fitted $v_{\rm in}$ is due to net inflow or to streaming motions (see §6.1), these changes are suggestive of resonance crossings.

4. In simulations the region around the CR is depopulated due to torques, as well as a lack of stable orbits between the CR and OLR in the case of strong bars. In NGC 4736 this is consistent with the gap in CO brightness around $r=30''$ and the gap in optical brightness from $r=200''$–$300''$ (Bosma et al. 1977).

On the other hand, our pattern speed for the nuclear bar conflicts with evidence from dynamical simulations (e.g., Tagger et al. 1987) that for nested bars the ILR of the outer bar corresponds to the CR of the inner bar. If this were the case in NGC 4736, it would be harder to understand the apparent outflow between the bar and the ring, unless the ring is sandwiched between two ILRs of the oval (Combes 1988), which is questionable (an inner ILR tends to occur where the rotation curve flattens, which for this galaxy is well inside the ring) but not ruled out by the present data. A stronger constraint could perhaps be provided by a dynamical (e.g. N-body) simulation of the galaxy, but such modeling is beyond the scope of this paper.

An intriguing alternative possibility, suggested by the threefold symmetry evident in the CO distribution, is that the ring corresponds to both the ILR of the oval and the outer 3:1 resonance of the bar, where $\Omega_p = \Omega + \kappa/3$. In this scenario, the arc-like features at the bar ends would occur at the inner 3:1 resonance, and the absence of threefold symmetry outside the zone between these resonances indicates that the $m=3$ waves do not propagate beyond them (Elmegreen et al. 1992). It is unclear how the direction of radial streaming motions (discussed in item 3 above) would change in such a model.

As bars are a convenient way to transport angular momentum outward so material can accrete toward the center (Friedli & Benz 1993), the existence of nested bars may provide a solution to the problem of fueling nuclear activity in galaxies (Shlosman et al. 1989), although observations to date do not show a significant tendency for active galaxies to contain bars (Ho, Filippenko, & Sargent 1997; Mulchaey & Regan 1997). In such a "bar-within-bar" scenario, gas brought in to the ILR of the outer bar could be driven in further by a rapidly rotating inner bar. However, since the inner bar can only bring in material that is already inside its CR, for our adopted pattern speed ($OLR_s=ILR_p$) it cannot draw in material from the ILR ring of the outer bar. Rather, it adds material to the ring by depleting gas near its CR. We speculate that this may be a general property of double-barred galaxies with strong rings, whereas in systems with pattern speeds such that $CR_s=ILR_p$, gas may continue on toward the nucleus instead of collecting in a ring.

## 6.3. Molecular Gas and Star Formation

### 6.3.1. Azimuthal differences in the ring

The results of §5 clearly indicate that the link between molecular gas and massive star formation in NGC 4736 is not as tight as might naïvely be expected. The contrast in the morphologies of CO and H$\alpha$ along the ring

is difficult to account for in terms of patchy extinction or local variations in the X-factor, as the CO and Hα distributions display fundamentally different symmetries. It is also difficult to attribute to recent changes in the $H_2$ distribution, since the OB stars responsible for the Hα emission are $\lesssim 10$ Myr old, which is less than the orbital timescale (20–30 Myr). Here we consider the possibility that certain locations in the ring are more conducive to the formation of massive stars, irrespective of the total gas content in these regions.

Why would massive stars preferentially form in certain locations in the ring? A recent study by Crocker, Baugus, & Buta (1996) of 32 ringed galaxies revealed a tendency for H II regions in intrinsically oval rings to be "bunched up" along the major axis of the ring, presumably where gas slows down in its orbits. Using our assumed disk parameters and the parameters of the ring given by MMG95, the intrinsic major axis of the ring has a PA of 320° in the sky, which appears to be too large to account for the concentration of Hα emission at PA 260°–305°. A second mechanism for producing strongly bisymmetric star formation in rings is the crowding together of gas in orbits associated with the bar and ring respectively to produce a "twin peaks" morphology (Kenney et al. 1992). Star formation would then be enhanced in these gas concentrations. This picture may be more appropriate for NGC 4736: the bright H II regions west of the nucleus are just downstream of where the outer CO arm (which may trace orbits associated with the oval distortion) intersects the ring (Figure 19). Either of these mechanisms could be aided by the tendency for a self-gravitating ring to collapse azimuthally as well as radially: Elmegreen (1994) has analyzed the growth of azimuthal perturbations in a magnetic ring and found that the fastest growing wavelength is roughly 4 times the radial thickness of the ring.

In all of these scenarios, however, peaks in molecular gas are expected to correspond to peaks in star formation, so the problem of the different azimuthal symmetries in CO and Hα remains unresolved. One solution for NGC 4736 would be for the distribution of *dense* molecular gas, as traced by HCN(1–0) emission, to resemble the bisymmetric Hα distribution rather than the CO, since star formation will presumably be concentrated in the densest gas. In NGC 6951, for instance, Kohno, Kawabe, & Vila-Vilaró (1999) found that the HCN peaks are shifted downstream of the CO peaks, and agree better with the positions of Hα and radio continuum emission than the CO does. To investigate this possibility for NGC 4736, relatively deep observations will be needed: short BIMA observations at $18''$ resolution detect no HCN emission at a $3\sigma$ upper limit of 0.15 Jy bm$^{-1}$ (0.1 K).

Alternatively, the triggering of massive star formation may be enhanced by the compression or collision of gas clouds, as has been suggested by Scoville, Sanders, & Clemens (1986). Since star formation is observed to be an inefficient process (Myers et al. 1986), the total gas mass may be less important if forces besides self-gravity can aid in collapse. In starburst rings, convergent gas flow in regions where streamlines intersect may provide the necessary trigger, resulting in the formation of unusually compact clusters (e.g. Barth et al. 1995). Whether cloud collisions tend to lead to the formation of gravita-

tionally bound clouds or to cloud disruption is a controversial issue (Larson 1988), but simulations of cloud collisions which take into account the clumpy structure of molecular clouds succeed in producing gravitational instabilities (Kimura & Tosa 1996). The notion that gas kinematics can affect the SFE is also in accord with star formation patterns observed in galactic bars (see §6.3.2 below) and merging galaxies (Mihos, Bothun, & Richstone 1993).

### 6.3.2. *Radial differences*

The lack of star formation interior to the ring, despite the large quantities of molecular gas in the inner disk, is not predicted by Schmidt-type laws ($\Sigma_{\text{SFR}} \propto \Sigma_{\text{gas}}^N$), or even alternative formulations where the SFR scales with the orbital frequency (Wyse & Silk 1989) or the stellar surface density (Dopita & Ryder 1994), both of which peak toward the center. As discussed in §3.2, radial variations in the X-factor due to a metallicity gradient may lead us to overestimate the $H_2$ mass in this region, but for a realistic metallicity gradient this is unlikely to lead to the sharp rise in $\tau_{\text{gas}}$ observed inside the ring (Figure 18). While a dramatic increase in extinction is possible, in §5.1 we argued that obscured massive star formation was unlikely to be widespread in the inner disk. Here we consider three other factors which could strongly affect either the SFE or the X-factor in the inner disk: (1) inhibition of star formation due to the kinematic effects of the bar; (2) a high critical density for gravitational instability; or (3) a change in both the X-factor and star formation efficiency due to increased velocity dispersions.

1. A depressed level of star formation along galactic bars has been noted for some time (for recent work see Phillips 1996), with massive star formation tending to concentrate at the bar ends or in circumnuclear rings, especially in early-type galaxies. Tubbs (1982) has suggested that star formation is inhibited along bars because clouds are disrupted when they hit the bar shock. Alternatively, the short orbital timescales in the vicinity of the nuclear bar may prevent clouds from collapsing gravitationally before being driven apart by diverging streamlines as they exit the bar. Observations of the galaxies NGC 1097 and NGC 6574, both of which contain abundant molecular gas associated with a nuclear bar but relatively little star formation (Kotilainen et al. 2000), also point to the presence of a bar being a key factor.

2. The deficit of star formation in the inner disk may be related to the large critical density for gravitational instability ($\Sigma_{\text{crit}}$). This density typically increases towards a galaxy's center due to the stabilizing effects of rapid rotation, and can lead to very large gas densities being required before star formation is triggered. Once star formation commences, it proceeds at a rapid rate due to the nonlinearity of the Schmidt law, creating a nuclear starburst (Kennicutt 1989). The large values of $Q$ in the nuclear region of NGC 4736, as well as evidence for a past starburst, are consistent with this scenario. Of course, $Q$ may not be a good measure of gravita-

tional instability in the vicinity of a bar where the potential is far from axisymmetric.

3. The CO(1–0) line may have low to moderate ($\tau \sim 1$) optical depth, due to high velocity dispersions (and possibly excitation temperatures) in the molecular gas. Such a situation has been inferred in the Galactic Center by Dahmen et al. (1998) based on large $^{12}CO/C^{18}O$ ratios, and a similar conclusion was reached by Aalto et al. (1995) for the central regions of starburst galaxies. High velocity dispersions are especially likely in the vicinity of a nuclear bar. A low CO optical depth will result in the CO intensity overestimating the $H_2$ column density when a standard X-factor is applied. Furthermore, since high velocity dispersions would raise the virialization density, there is likely to be a greater fraction of CO emission that is not associated with virialized clouds and is hence unrelated to star formation. Both of these factors would contribute to the high CO/H$\alpha$ ratio in the inner disk of NGC 4736.

All of these explanations seem plausible based on the existing evidence. Further studies of nuclear and ring starbursts would be useful for understanding what factors are most important in triggering or inhibiting star formation near the nucleus. The recent work of Jogee (1999), for instance, suggests that the suppression of star formation in regions of strong non-circular kinematics may be quite common. In addition, much remains to be learned about how star formation occurs in barred galaxies and in the Galactic Center, and high-resolution observations of $^{13}CO$ in NGC 4736 should be undertaken to probe the conditions of the molecular gas in both the inner disk and the ring.

## 6.4. *Atomic Gas and Star Formation*

The similarities in the H I and H$\alpha$ radial (§5.5) and azimuthal (§5.3) distributions in the ring, where most of the gas is molecular, suggest that H I there is largely a product of $H_2$ dissociation. Similar conclusions have been reached for the grand-design spiral galaxies M51 (Vogel et al. 1988; Tilanus & Allen 1989) and M83 (Allen, Atherton, & Tilanus 1986), in regions where the ISM is also predominantly molecular. On the other hand, the azimuthal profiles of H I and H$\alpha$ do not agree in detail, even though both are bisymmetric. This may result from the depletion of H I in favor of H II near the brightest H II regions, or the presence of an older stellar component in the ring that contributes to photodissociation but not photoionization. A direct probe of photodissociation regions is provided by observations of the [C II] line at 158 $\mu$m, which Stacey et al. (1991) have used to argue that photodissociated gas constitutes a large fraction of the gas mass in star-forming galaxies. However, the resolution of their observations ($55''$) was too low to allow a detailed comparison of [C II] and H I. Future high-resolution observations of [C II] by the SOFIA airborne observatory will provide a strong test of this model.

If this interpretation is correct, then the strong correlation between the H I surface density ($\Sigma_{HI}$) and SFR per unit area ($\Sigma_{SFR}$) found in this study and in previous work

(Kennicutt 1998a, and references therein) is simply a result of the H I being produced by star formation (Shaya & Federman 1987). This may only apply in the inner, $H_2$ dominated regions of massive spirals: in the outer regions the preferred phase for the neutral gas will be atomic (e.g., Elmegreen 1993), and one would expect the formation of dense H I clouds to precede (rather than follow) the formation of molecular clouds and stars, as is apparently the case in the Perseus arm of our Galaxy (Heyer & Terebey 1998). Hence the correlation between H I and SFR should break down in the outer parts of disks, which may explain why the correlation between the *total* H I content and SFR in galaxies is comparatively poor (Young et al. 1989).

## 6.5. *Star Formation at Subcritical Gas Densities*

As shown in §5.4, massive star formation in NGC 4736 appears to be occurring at gas densities that, when azimuthally averaged, are a factor of $\sim$3 below the expected threshold density for gravitational instability. A similar conclusion had been tentatively reached by Shioya et al. (1998) based on lower resolution data. Hence star formation is evidently quite vigorous at $Q \sim 3$, whereas Kennicutt (1989) found for his sample that star formation was suppressed when $Q > 1.5$. Previous studies of the low surface brightness galaxies M33 (Wilson, Scoville, & Rice 1991) and NGC 2403 (Thornley & Wilson 1995) have also found star formation occurring at "subcritical" gas densities, but in contrast NGC 4736 is a bright, early-type galaxy.

One should bear in mind, however, that the derived value of $Q$ is subject to considerable uncertainty because it is the product of several measured quantities. Since $Q \propto \kappa \sigma_v / \Sigma_{gas}$, we could overestimate it by overestimating $\kappa$ or $\sigma_v$ or underestimating $\Sigma_{gas}$. The errors in $\kappa$ are formally $\sim$30%, but they are harder to quantify for $\sigma_v$ from our rough analysis (although $\sigma_v \ll 7$ km s$^{-1}$ seems unrealistic) and largely unknown for $\Sigma_{gas}$, which relies on the X-factor. Since comparable or greater uncertainties are likely to exist for the data used by Kennicutt (1989), a factor of $\sim$2 discrepancy between our results may not be particularly meaningful.

Even if the basic $Q < 1$ criterion does break down in this galaxy, this need not imply that star formation has occurred in regions that were gravitationally stable. Rather, it may just be an indication that a one-parameter model is an incomplete description of how gravitational instability ultimately leads to star formation. As mentioned in §5.4, there are molecular condensations in the ring where $Q < 1$ locally. Such condensations probably resulted from processes other than axisymmetric gravitational instability, but their subsequent collapse to form stars may still be governed in part by $Q$. Moreover, the derivation of $Q$ assumes a thin isothermal one-component disk; more realistic models show that the interaction of gas and stars creates greater instability (Jog & Solomon 1984; Elmegreen 1995). Finally, we emphasize that there remains considerable uncertainty about the physical basis for the $Q$ threshold (see e.g. Larson 1988), in particular whether it is in fact related to an axisymmetric instability ($Q$ threshold $\sim 1$) or to swing amplification of density waves ($Q$ threshold 1–2).

Considering both the observational and theoretical un-

certainties, it is remarkable how well the location of the dip in $Q$ matches the location of the ring (Figure 21). We conclude that our data support the general picture of a link between star formation and gravitational instability in NGC 4736, although with some uncertainty in the exact value of the $Q$ threshold. However, firm conclusions on the general applicability of the star formation threshold can only be drawn once a large sample of galaxies has been examined in detail.

### 6.6. *Radial Gas Flows and Galaxy Evolution*

Star formation is occurring in the ring at a rate which can only be sustained for $\sim 1$ Gyr (Figure 18). In fact, Figure 18 already gives some indication that substantial gas consumption has occurred, in that the positions of the CO and H$\alpha$ rings are not coincident. Based on the current SFR, roughly 0.2 M$_\odot$ yr$^{-1}$ of additional gas needs to be added to the ring ($30'' < r < 60''$) to replenish the gas used by star formation (Smith et al. 1991). (This is probably a lower limit since extinction has not been taken into account in deriving the SFR.) This level of refueling could be accomplished by an outflow velocity of approximately 1 km s$^{-1}$ at $r=30''$ or a comparable inflow velocity at $r=60''$, based on the gas surface densities at those radii. One can equivalently view this as the inflow velocity required to build up the ring on a timescale of $\sim 1$ Gyr, in the absence of star formation. Note that replenishment requires much smaller radial flows than those predicted by the radial inflow model (Figure 15), which would tend to rapidly build up the ring.

Our estimate of the gas consumption time is admittedly simplistic, since it neglects the effects of stellar recycling, which can increase gas consumption times by factors of $\sim 2$ (Kennicutt et al. 1994), and is quite sensitive to uncertainties in the IMF, extinction, X-factor, etc. However, it does indicate that even small radial flow rates can have a dramatic impact on extending the lifetimes of star-forming rings. Thus, as long as bars continue to drive radial gas flows, star formation in rings can probably continue indefinitely. The mass concentration in the ring inferred from the rotation curve (§4.1) indicates that it is not a very young feature. On the other hand, it does not appear old enough to have strongly affected the $K$-band light profile (§3.2). A detailed photometric study aimed at determining the approximate age of the ring, as has been performed by Buta (1991) for NGC 7702, would be quite useful in understanding its evolution.

How did a strong central peak in the H$_2$ surface density arise, if gas inflow stops at the ring (ILR)? Continued mass loss from stars in the bulge may build up significant amounts of gas, which the nuclear bar then redistributes toward the ring and nucleus. Star formation might be active in the ring because of the lower critical density (small $\kappa$) there, but be sporadic at the nucleus because the critical density there is much higher. This is consistent with the spectroscopic evidence that the nucleus has undergone a recent starburst event. Alternatively, gas could have been driven directly into the central region by the oval early in its evolution, before matter became centrally concentrated enough to produce an ILR.

### 7. CONCLUSIONS

We have presented an analysis of CO, H I, and H$\alpha$ data for the ringed galaxy NGC 4736. Our main results can be summarized as follows:

*Gas distribution.*—A molecular counterpart is seen to the nuclear stellar bar, as has been previously reported by Sakamoto et al. (1999). Arm-like extensions from the bar ends, probably associated with a spiral dust arc seen in color index maps, connect the inner molecular disk with the star-forming ring, which is associated with tightly wound CO arms. Overall, the distribution of neutral gas appears to be dominated by H I outside the ring and H$_2$ interior to the ring. The H I intensity along the ring shows a strong twofold symmetry which is completely lacking in the CO. Instead, the CO shows indications of a threefold symmetry, both in the ring and the inner disk. The radial distribution of gas does not follow a simple exponential but shows distinct humps, possibly due to mass redistribution by radial flows. The stellar profile derived from a $K$-band image is steeper than the gas profile within $r=60''$.

*Gas kinematics.*—The rotation curve is consistent with a scenario in which the ring corresponds to the OLR of the nuclear bar and the ILR of the large-scale oval distortion. Such a coupling of nested bars may contribute to the accumulation of gas in the ring. The directions of radial gas flow suggested by the velocity residuals are also in good agreement with this picture. The influence of the nuclear bar on the kinematics of the inner disk is readily apparent in the CO velocity residuals, which show the expected $\cos 3\theta$ signature for streaming in aligned elliptical orbits. The H I velocity residuals outside the ring do not show this signature, resembling instead a model of uniform radial inflow. However, the very high ($\sim 40$ km s$^{-1}$) inflow velocities inferred raise difficulties for this model as well. A more realistic model in which elliptical orbits are precessed (i.e., change orientation with radius) may warrant further study.

*Star formation.*—The radial distributions of CO and H$\alpha$ are radically different and are consistent with a simple Schmidt law only when the inner CO disk is excluded. Some possible explanations for this discrepancy are inhibition of star formation in the vicinity of the nuclear bar, a high threshold density for gravitational instability in the central regions, or a change in the X-factor related to a change in CO(1–0) opacity. The correlation between H I and H$\alpha$ emission and their similar azimuthal profiles suggest that H I may be largely a product of H$_2$ dissociation, at least in regions that are dominated by molecular gas. We find that the Toomre $Q$ parameter has a local minimum of $\sim 3$ at the location of the star-forming ring, when derived from azimuthally averaged gas densities. This minimum is in general agreement with the theory in which star formation is initiated by global gravitational instabilities, although $Q$ is expected to be a factor of $\sim 2$ smaller than observed. The azimuthal H$\alpha$ profile, unlike the CO profile, displays a strong twofold symmetry, indicating that massive star formation is enhanced at certain locations in the ring, independent of the molecular gas mass. Such locations may be associated with dense gas not traced by CO or with convergent gas flows. We conclude that the star formation rate is not determined solely by the available gas mass, but rather that large-scale dynamics play a significant role in organizing and possibly

triggering star formation.

## REFERENCES

Aalto, S., Booth, R. S., Black, J. H., & Johansson, L. E. B. 1995, A&A, 300, 369
Allen, R. J., Atherton, P. D., & Tilanus, R. P. J. 1986, Nature, 319, 296
Athanassoula, E. 1992, MNRAS, 259, 345
Barth, A. J., Ho, L. C., Filippenko, A. V., & Sargent, W. L. W. 1995, AJ, 110, 1009
Becker, R. H., White, R. L., & Helfand, D. J. 1995, ApJ, 450, 559
Begeman, K. G. 1989, A&A, 223, 47
Benedict, G. F., Smith, B. J., & Kenney, J. D. P. 1996, AJ, 111, 1861
Block, D. L., Bertin, G., Stockton, A., Grosbøl, P., Moorwood, A. F. M., & Peletier, R. F. 1994a, A&A, 288, 365
Block, D. L., Witt, A. N., Grosbøl, P., Stockton, A., & Moneti, A. 1994b, A&A, 288, 383
Bloemen, J. B. G. M., Strong, A. W., Mayer-Hasselwander, H. A., Blitz, L., Cohen, R. S., Dame, T. M., Grabelsky, D. A., Thaddeus, P., Hermsen, W., & Lebrun, F. 1986, A&A, 154, 25
Bohlin, R. C., Savage, B. D., & Drake, J. F. 1978, ApJ, 224, 132
Bosma, A. 1978, PhD thesis, Univ. of Groningen
Bosma, A., van der Hulst, J. M., & Sullivan, W. T. 1977, A&A, 57, 373
Braun, R. 1995, A&AS, 114, 409
—. 1997, ApJ, 484, 637
Briggs, D. 1995, PhD thesis, New Mexico Inst. of Mining and Tech.
Burton, W. B. & Liszt, H. S. 1978, ApJ, 225, 815
Buta, R. 1988, ApJS, 66, 233
—. 1991, ApJ, 370, 130
Buta, R. & Combes, F. 1996, Fund. Cosmic Phys., 17, 95
Byrd, G., Rautiainen, P., Salo, H., Buta, R., & Crocker, D. A. 1994, AJ, 108, 476
Combes, F. 1988, in Galactic and Extragalactic Star Formation, ed. R. E. Pudritz & M. Fich (Dordrecht: Kluwer), 475
Combes, F. & Gerin, M. 1985, A&A, 150, 327
Contopoulos, G., Gottesman, S. T., Hunter, J. H., & England, M. N. 1989, ApJ, 343, 608
Crocker, D. A., Baugus, P. D., & Buta, R. 1996, ApJS, 105, 353
Cui, W., Feldkhun, D., & Braun, R. 1997, ApJ, 477, 693
Dahmen, G., Hüttemeister, S., Wilson, T. L., & Mauersberger, R. 1998, A&A, 331, 959
de Vaucouleurs, G. & Buta, R. 1980, ApJS, 44, 451
de Vaucouleurs, G., de Vaucouleurs, A., Corwin, H. G., Buta, R. J., Paturel, G., & Fouqué, P. 1991, Third Reference Catalogue of Bright Galaxies (New York: Springer-Verlag)
Dopita, M. A. 1985, ApJ, 295, L5
Dopita, M. A. & Ryder, S. D. 1994, ApJ, 430, 163
Duric, N. & Dittmar, M. R. 1988, ApJ, 332, L67
Elmegreen, B. G. 1993, ApJ, 411, 170
—. 1994, ApJ, 425, L73
—. 1995, MNRAS, 275, 944
Elmegreen, B. G., Elmegreen, D. M., & Montenegro, L. 1992, ApJS, 79, 37
Friedli, D. & Benz, W. 1993, A&A, 268, 65
Friedli, D. & Martinet, L. 1993, A&A, 277, 27
Gerin, M., Casoli, F., & Combes, F. 1991, A&A, 251, 32
González Delgado, R. M. et al. 1997, ApJS, 108, 155
Heckman, T. M. 1980, A&A, 87, 152
Heyer, M. H. & Terebey, S. 1998, ApJ, 502, 265
Ho, L. C., Filippenko, A. V., & Sargent, W. L. W. 1997, ApJ, 487, 591
Huchtmeier, W. K. & Seiradakis, J. H. 1985, A&A, 143, 216
Jog, C. J. & Solomon, P. M. 1984, ApJ, 276, 114
Jogee, S. 1999, PhD thesis, Yale University

Kenney, J. D. P. 1994, in Mass-Transfer Induced Activity in Galaxies, ed. I. Shlosman (Cambridge: Cambridge U. Press), 78
Kenney, J. D. P. 1997, in The Interstellar Medium in Galaxies, ed. J. M. van der Hulst (Dordrecht: Kluwer), 33
Kenney, J. D. P., Carlstrom, J. E., & Young, J. S. 1993, ApJ, 418, 687
Kenney, J. D. P., Scoville, N. Z., & Wilson, C. D. 1991, ApJ, 366, 432
Kenney, J. D. P., Wilson, C. D., Scoville, N. Z., Devereux, N. A., & Young, J. S. 1992, ApJ, 395, L79
Kennicutt, R. C. 1989, ApJ, 344, 685
—. 1998a, ApJ, 498, 541
—. 1998b, ARA&A, 36, 189
Kennicutt, R. C., Tamblyn, P., & Congdon, C. W. 1994, ApJ, 435, 22
Kimura, T. & Tosa, M. 1996, A&A, 308, 979
Kohno, K., Kawabe, R., & Vila-Vilaró, B. 1999, ApJ, 511, 157
Kormendy, J. 1982, in Morphology and Dynamics of Galaxies, ed. L. Martinet & M. Mayor (Sauverny: Geneva Obs.), 113
Kotilainen, J. K., Reunanen, J., Laine, S., & Ryder, S. D. 2000, A&A, 353, 834
Kutner, M. L. & Ulich, B. L. 1981, ApJ, 250, 341
Laine, S., Shlosman, I., & Heller, C. H. 1998, MNRAS, 297, 1052
Larson, R. 1988, in Galactic and Extragalactic Star Formation, ed. R. E. Pudritz & M. Fich (Dordrecht: Kluwer), 459
Liszt, H. S. & Burton, W. B. 1980, ApJ, 236, 779
Louis, P. D. & Gerhard, O. E. 1988, MNRAS, 233, 337
Maoz, D., Filippenko, A. V., Ho, L. C., Rix, H.-W., Bahcall, J. N., Schneider, D. P., & Macchetto, F. D. 1995, ApJ, 440, 91
Mihos, J. C., Bothun, G. D., & Richstone, D. O. 1993, ApJ, 418, 82
Möllenhoff, C., Matthias, M., & Gerhard, O. E. 1995, A&A, 301, 359 (MMG95)
Mulchaey, J. S. & Regan, M. W. 1997, ApJ, 482, L135
Mulder, P. S. 1995, A&A, 303, 57
Mulder, P. S. & van Driel, W. 1993, A&A, 272, 63
Myers, P. C., Dame, T. M., Thaddeus, P., Cohen, R. S., Silverberg, R. F., Dwek, E., & Hauser, M. G. 1986, ApJ, 301, 398
Oey, M. S. & Kennicutt, R. C. 1993, ApJ, 411, 137
Phillips, A. C. 1996, in Barred Galaxies, ASP Conference Series Vol. 91, ed. R. Buta, D. A. Crocker, & B. G. Elmegreen (San Francisco: ASP), 44
Pogge, R. W. 1989, ApJS, 71, 433
Pritchet, C. 1977, ApJS, 35, 397
Quillen, A. C., Frogel, J. A., Kenney, J. D. P., Pogge, R. W., & DePoy, D. L. 1995, ApJ, 441, 549
Quirk, W. J. 1972, ApJ, 176, 9
Regan, M. W., Vogel, S. N., & Teuben, P. J. 1997, ApJ, 482, L143
Rieke, G. H. & Lebofsky, M. J. 1985, ApJ, 288, 618
Roberts, W. W. 1969, ApJ, 158, 123
Roche, P. F. & Aitken, D. K. 1985, MNRAS, 213, 789
Safranov, V. S. 1960, Ann. d'Ap., 23, 979
Sakamoto, K., Okumura, S., Minezaki, T., Kobayashi, Y., & Wada, K. 1995, AJ, 110, 2075
Sakamoto, K., Okumura, S. K., Ishizuki, S., & Scoville, N. Z. 1999, ApJS, 124, 403
Sandage, A. 1961, The Hubble Atlas of Galaxies (Washington, D.C.: Carnegie Inst. of Washington)
Sanders, R. H. & Huntley, J. M. 1976, ApJ, 209, 53
Sanders, R. H. & Tubbs, A. D. 1980, ApJ, 235, 803

Sault, R. J., Teuben, P. J., & Wright, M. C. H. 1995, in Astronomical Data Analysis Software and Systems IV, ASP Conference Series Vol. 77, ed. R. A. Shaw, H. E. Payne, & J. J. E. Hayes (San Francisco: ASP), 433

Schmidt, M. 1959, ApJ, 129, 243

Schwarz, M. P. 1981, ApJ, 247, 77

Scoville, N. Z., Sanders, D. B., & Clemens, D. P. 1986, ApJ, 310, L77

Shaya, E. J. & Federman, S. R. 1987, ApJ, 319, 76

Shioya, Y., Tosaki, T., Ohyama, Y., Murayama, T., Yamada, T., Ishizuki, S., & Taniguchi, Y. 1998, PASJ, 50, 317

Shlosman, I., Frank, J., & Begelman, M. C. 1989, Nature, 338, 45

Shu, F. H., Milione, V., & Roberts, W. W. 1973, ApJ, 183, 819

Simkin, S. M., Su, H. J., & Schwarz, M. P. 1980, ApJ, 237, 404

Smith, B. J., Lester, D. F., Harvey, P. M., & Pogge, R. W. 1991, ApJ, 373, 66

Sodroski, T. J. et al. 1995, ApJ, 452, 262

Stacey, G. J., Geis, N., Genzel, R., Lugten, J. B., Poglitsch, A., Sternberg, A., & Townes, C. H. 1991, ApJ, 373, 423

Stanimirović, S., Staveley-Smith, L., Dickey, J. M., Sault, R. J., & Snowden, S. L. 1999, MNRAS, 302, 417

Steer, D. G., Dewdney, P. E., & Ito, M. R. 1984, A&A, 137, 159

Strong, A. W. & Mattox, J. R. 1996, A&A, 308, L21

Tagger, M., Sygnet, J. F., Athanassoula, E., & Pellat, R. 1987, ApJ, 318, L43

Teuben, P. 1991, in Warped Disks and Inclined Rings Around Galaxies, ed. S. Casertano, P. D. Sackett, & F. H. Briggs (Cambridge: Cambridge U. Press), 40

Teuben, P. J. 1995, in Astronomical Data Analysis Software and Systems IV, ASP Conference Series Vol. 77, ed. R. A. Shaw, H. E. Payne, & J. J. E. Hayes (San Francisco: ASP), 398

Thornley, M. D. & Wilson, C. D. 1995, ApJ, 447, 616

Tilanus, R. P. J. & Allen, R. J. 1989, ApJ, 339, L57

Toomre, A. 1964, ApJ, 139, 1217

Tubbs, A. D. 1982, ApJ, 255, 458

Turner, J. L. & Ho, P. T. P. 1994, ApJ, 421, 122

van der Hulst, J. M., Terlouw, J. P., Begeman, K., Zwitser, W., & Roelfsema, P. R. 1992, in Astronomical Data Analysis Software and Systems I, ASP Conference Series Vol. 25, ed. D. M. Worall, C. Biemesderfer, & J. Barnes (San Francisco: ASP), 131

van der Kruit, P. C. 1976, A&A, 52, 85

van der Kruit, P. C. & Allen, R. J. 1978, ARA&A, 16, 103

van der Kruit, P. C. & Shostak, G. S. 1984, A&A, 134, 258

Vogel, S. N., Kulkarni, S. R., & Scoville, N. Z. 1988, Nature, 334, 402

Walker, C. E., Lebofsky, M. J., & Rieke, G. H. 1988, ApJ, 325, 687

Walterbos, R. A. M. & Braun, R. 1996, in The Minnesota Lectures on Extragalactic Neutral Hydrogen, ASP Conference Series Vol. 106, ed. E. D. Skillman (San Francisco: ASP), 1

Wilson, C. D. 1995, ApJ, 448, L97

Wilson, C. D., Scoville, N. Z., & Rice, W. R. 1991, AJ, 101, 1293

Wong, T. 2000, PhD thesis, Univ. of California at Berkeley

Wong, T. & Blitz, L. 1999, Ap&SS, in press

Wyse, R. F. G. & Silk, J. 1989, ApJ, 339, 700

Young, J. S., Xie, S., Kenney, J. D. P., & Rice, W. L. 1989, ApJS, 70, 699